Dyke emplacement and crustal structure within a continental large igneous province - northern Barents Sea

Alexander Minakov[1,4], Viktoriya Yarushina[2], Jan Inge Faleide[1], Nataliya Krupnova[3], Tamara Sakoulina[3], Nikolay Dergunov[3], Vladimir Glebovsky[5]

[1]Centre for Earth Evolution and Dynamics (CEED), University of Oslo, NO-0315 Oslo, Norway

[2]Institute for Energy Technology (IFE), NO-2007 Kjeller, Norway

[3]JSC Sevmorgeo Rosnedra, 198095 St. Petersburg, Russia

[4]VISTA, Norwegian Academy of Science and Letters, N-0271 Oslo, Norway

[5]VNIIOkeangeologia, 190121 St. Petersburg, Russia

Abstract: We perform an integrated analysis of magnetic anomalies, multichannel seismic and wide-angle seismic data across an Early Cretaceous continental large igneous province in the northern Barents Sea region. Our data show that the high-frequency and high-amplitude magnetic anomalies in this region are spatially correlated with dykes and sills observed onshore. The dykes are group in two conjugate swarms striking oblique to the northern Barents Sea passive margin in the eastern Svalbard and Franz Josef Land regions, respectively. The multichannel seismic data east of Svalbard and south of Franz Josef Land indicate the presence of sills at different stratigraphic levels. The most abundant population of sills is observed in the Triassic successions of the East Barents Sea Basin. We observe near-vertical seismic column-like anomalies that cut across the entire sedimentary cover. We interpret these structures as magmatic feeder channels or dykes. In addition, the compressional seismic velocity model locally indicates nearly vertical positive finger-shaped velocity anomalies (10-15 km wide) that extend to mid-crustal depths (15-20 km) and possibly deeper. The crustal structure does not include magmatic underplating and shows no regional crustal thinning suggesting a localized (dyking, channelized flow) rather than pervasive mode of magma emplacement. We suggest that most of crustal extension was taken up by brittle-plastic dilatation in shear bands. We interpret the geometry of dykes in the horizontal plane in terms of the palaeo-stress regime using a model of a thick elastoplastic plate containing a circular hole (at the plume location) and subject to combined pure shear and pressure loads. The geometry of dykes in the northern Barents Sea and Arctic Canada can be predicted by the pattern of dilatant plastic shear bands obtained in our numerical experiments assuming boundary conditions consistent with a combination of extension in the Amerasia Basin sub-parallel to the northern Barents Sea margin and a mild compression nearly orthogonal to the margin. The approach has implications for palaeo-stress analysis using geometry of dyke swarms.

1 Introduction

A large number of continental large igneous provinces (LIPs) were formed throughout Earth history (Coffin & Eldholm 1994, Ernst 2014). A typical LIP event is associated with eruption of over 10^6 km^3 of basalts. This massive eruption of flood basalts and corresponding intrusive components are attributed to a temperature and melting anomaly in the mantle due to plumes (Richards *et al.* 1989; White & McKenzie 1995). The main eruptive phase of flood basalts is geologically short and lasts typically 1-5 million years (Jerram & Widdowson 2005, Svensen *et al.* 2012). LIPs are closely linked to continental breakup (Buiter & Torsvik 2014). The effect of magmatic weakening and magma-assisted breakup is pronounced on the central Atlantic (Hames *et al.* 2000) and northeast Atlantic margins (Eldholm & Grue 1994), East-African rift (Ebinger & Casey 2001, Buck 2006, Kendall *et al.* 2005), and India-Seychelles margins (Minshull *et al.* 2008).

Giant radiating dyke swarms are often associated with LIPs and can be used as markers to reconstruct the pre-breakup position of the continents (Ernst *et al.* 2013). The orientation of dykes can also be used to infer palaeo-stress regime on pre-breakup continental margins (Hou *et al.* 2010). On the other hand, existing models for formation of giant dyke swarms are partly based on Venusian analogues (associated with coronae structures) since on Earth the entire palaeo-structures are less likely to be preserved due to erosion and plate tectonics (McKenzie *et al.* 1992). The lack of structural constraints and complex geometry of giant dyke swarms has promoted debates on physical mechanisms behind their formation and the role played by mantle plumes (e.g. McHone *et al.* 2005). With this contribution, we address the mechanical aspects of genesis and geometry of giant dyke swarms and the key role of rheological behaviour of the lithosphere affected by a mantle plume.

A giant radiating dyke swarm has been identified in the Arctic region by Buchan & Ernst (2006) in the circum-Arctic continental shelves. This has supported the existence of the High Arctic LIP-related magmatic event (Lawver & Muller 1994, Tarduno 1998, Maher 2001) previously inferred from a number of structural and lithological observations including geochemistry of basalts (Bailey & Rasmussen 1997, Ntaflos & Richter 2003, Drachev & Saunders 2006). The later analysis of detailed aeromagnetic data (Minakov *et al.* 2012a, Døssing *et al.* 2013) and analysis of multichannel and wide-angle seismic profiles (Grogan *et al.* 2000, Minakov *et al.* 2012a, Polteau *et al.* 2016) suggested significant intrusive component of the High Arctic LIP in the Barents Sea.

The lack of vegetation and perfect exposure in the islands of the northern Barents Sea region allows for unique correlation of geophysical data and onshore geology. In Franz Josef Land most dykes are near vertical with a thickness that ranges between 2-30 meters but locally may increase to more than 100 meters (Dibner 1998). Basalt flows are typically 2-70 meters thick, locally up to 100 meters with a total thickness of 200-350 m. From a geochemical point of view two major groups were identified: low-potassium tholeiitic basalts and andesitic basalts (Ntaflos & Richter 2003, Dibner 1998).

Corfu *et al.* (2013) determined the crystallization ages of mafic sills in Svalbard and Franz Josef Land using U–Pb methods on different minerals. The ages obtained suggest a rapid magma emplacement in agreement with previous studies of other LIPs (Hames *et al.* 2000, Svensen *et al.* 2012). Their results indicate an age of ~124 Ma and ~122 Ma (with an accuracy within 1 Myr), for the sills in Svalbard and Franz Josef Land, respectively. $^{40}K/^{40}Ar$ and $^{40}Ar/^{39}Ar$ data (Nejbert et al. 2011, Shipilov & Karyakin 2011, Piskarev *et al.* 2009) indicate a much larger spread of ages (~200-90 Ma) with an uncertainty of some determinations of up to ±29 Myr (Shipilov & Karyakin 2011). The interpretation of these data in terms of the timing of dyke emplacement is not straightforward. The isotopic geochronology studies in other continental large igneous provinces has shown that the U-Pb dating technique generally better constrains the crystallization age of mafic intrusions compared to the K-Ar (and Ar-Ar) system that can be heavily affected by complex thermal history, extraneous argon, recoil loss, uncertainties in the ages of standards and other factors (e.g. Svensen *et al.* 2012)

In this study we reserve the term “High Arctic LIP” for the main intrusive phase of magmatism, postulated to be a result of the plume-lithosphere interaction that initiated continental breakup of the Arctic continental lithosphere (Lawver & Müller 1994, Drachev & Saunders 2006). We assume that the younger Late Cretaceous magmatism (70-100 Ma) in the west Arctic region (e.g. Tegner *et al.* 2011) can be related to lithosphere rifting. The proposed view is documented by a large dataset of geological and geophysical information in the Barents Sea. We reprocess and analyse magnetic data, seismic refraction, and multichannel seismic reflection data covering the dyke swarms in the northern Barents Sea. The data show no large amount of extension/rifting of continental lithosphere preceded the magmatism in the Barents Sea. The lack of Cenozoic faults or magmatism in the northern Barents Sea (Minakov *et al.* 2012b) makes possible to infer lithospheric stresses associated with the emplacement of the Early Cretaceous mafic dyke swarms by matching their geometry with results of mechanical modelling. The magnetic data reveal a radiating pattern of dykes crosscutting the Barents Sea shelf (Figs 1 & 2). We use these data as a rationale to discuss a possible mechanism of the dyke emplacement and predict the stress pattern related to early stages of the Amerasia Basin evolution. We briefly review existing models for the dyke geometry that are primarily based on elastic models. After that we draw attention to the phenomenon of dilatant plastic shear bands that, as we believe, controlled the geometry of dykes.

2 Geophysical data and processing

Seismic data

Seismic data were acquired by University of Bergen south-east of Kong Karls Land (Minakov *et al.* 2012a) and Joint Stock Company (JSC) Sevmorgeo in the eastern Barents Sea (Ivanova *et al.* 2011, Sakoulina *et al.* 2015) and combined to produce a composite deep seismic transect across the northern Barents Sea (Fig. 1). The western part (ESVA) consists of a 170 km long profile acquired in 2008 along which 14 ocean bottom seismometers were deployed. The acoustic source consisted of four equal-sized air guns with a total volume of about 80 litres that were fired every 200 meters. The processing of these data is described in Minakov *et al.* (2012a). The eastern part of the transect (4-AR) consists of a combined wide-angle and multichannel seismic reflection (MCS) profile, acquired in 2005-2006 that crosses the northern Barents Sea and the northernmost part of the Novaya Zemlya foldbelt (Ivanova *et al.* 2011, Sakoulina *et al.* 2015). The profile was acquired in 4 legs (240–500 km long each) and has total length of 1370 km. In this paper only a part of the profile is presented (140-1000 km). The ocean bottom seismic stations were deployed with a 10-km interval along 4-AR. The acoustic source consisted of a powerful single air gun with the chamber volume of about 120 litres. The shot interval was 250 meters. The data processing has been previously described in Ivanova *et al.* (2011) and Sakoulina *et al.* (2015).

We remodelled the western part of 4-AR using a combined reflection and refraction tomography method (Hobro & Singh 1999, Hobro *et al.* 2003). The profile was processed separately for the two segments: WNW-ESE part (140 – 500 km) and E-W part (500-1000 km). The first arrivals and Moho reflected travel times were picked after standard processing applied to recorded data including bandpass filtering, deconvolution, normalization of amplitudes by Ivanova *et al.* (2011) and Sakoulina *et al.* (2015). We performed the travel-time tomography using the JIVE3D code (Hobro & Singh 1999, Hobro *et al.* 2003). Using this approach the travel-time misfit function was optimized together with smoothness constraints to find a P-wave velocity model. A 1D starting model was constructed using previously published velocity models in the northern Barents Sea (Minakov *et al.* 2012a, Ivanova *et al.* 2011, Sakoulina *et al.* 2015). The forward problem solution was based on a ray perturbation method adopted from Fara & Madariaga (1987). The optimization problem was solved using iterative LSQR method (Paige & Saunders 1982). We used 30 nonlinear iterations to update the initial starting model. The uncertainty of picking was set to 100 ms beyond 30 km offset and 70 ms at closer distances. The final chi-square value was ~2.3 for the WNW-ESE segment and ~1.3 for the E-W segment, respectively. We attribute the increase of the chi squared value for the WNW-ESE segment to a complex three-dimensional velocity structure. The checkerboard resolution tests for both parts of the 4AR profile as well as the ray coverage, data residuals and traveltime plots can be found in Supplementray Material 1 & 2. In Fig. 3b & c, we show the velocity model, resulted from our tomographic inversion of Pg and PmP phases, together with the velocity model by Sakoulina *et al.* (2015) which is based on a forward modelling of all interpreted phases including secondary arrivals. The two models are in general agreement apart from minor discrepancies in the configuration of Moho.

The MCS survey along the 4-AR profile (Figs 4 & 5) was carried out by JSC Sevmorneftegeofizika in 2005 onboard RV "Akademik Lazarev". The airgun source consisted of 4258 cu. in. (69.8 litres) BOLT 1900 airguns. The SeaMUX 2000 seismic streamer was used as a receiver. The main acquisition parameters are provided in Table 1. The seismic data along the 4-AR profile were processed in JSC Sevmorgeo. The initial processing was performed using FOCUS software (Paradigm Geophysical) and presented in Ivanova *et al.* (2011).

In this work the data were reprocessed aiming to eliminate the surface-related multiple reflections. The re-processing of the 4-AR MCS data was performed using FOCUS and GeoDepth© software (Paradigm Geophysical). The processing sequence included: band-pass filtering, SRME multiple removal, velocity analysis, geometrical spreading amplitude correction, tau-p deconvolution, multiple suppression using Radon transform, spectral equalization and broadening of the spectrum.

The final processing step consisted of seismic migration applied to shot data both in time domain. We applied Kirchhoff pre-stack time migrationusing average (RMS) velocities. In addition, F-X and time-dependent deconvolution were applied to migrated seismic sections.

Magnetic anomalies

We compiled a magnetic anomaly map for the northern Barents Sea region (Fig. 2) including a 5x5 km grid extracted from the circum-Arctic CAMP compilation (Gaina *et al.* 2011) and 2x2 km grids for the Svalbard and Franz Josef Land regions. The aerogeophysical survey over Franz Josef Land was carried by the Polar Marine Geological Expedition (PMGRE) in 1997 and 1998-2000. The results of processing and interpretation of trackline data were presented in Verba *et al.* (2004), Glebovsky *et al.* (2006a,b), and Minakov *et al.* (2012b). The magnetic data over the Svalbard region were acquired by Sevmorgeo-PMGRE, TGS-NOPEC Geophysical Company and the Norwegian Geological Survey (NGU) in 1989-1991. The results of data processing and interpretation south and east of Svalbard can be found in Skilbrei (1991), Skilbrei (1992), and Olesen *et al.* (2010). The specifications of aeromagnetic data are placed in Table 2.

The profile aeromagnetic data over Franz Josef Land were re-processed in VNIIOkeangeologia including more accurate leveling procedures. The additional processing included the adjustment of the regional trends in the data. We used a 500-km Butterworth low-pass filter to extract a regional trend of magnetic anomalies from the CAMP grid. The corresponding long-wavelength component was removed from the local grids for Svalbard and Franz Josef Land areas and replaced by the trend derived from the CAMP grid.

3 Geological interpretations

In the following we present an integrated interpretation of seismic and magnetic data within the northern Barents Sea region with an emphasis on the geometry and distribution of mafic intrusions. The study region is composed of the Kong Karls Land platform (a Permian-Carboniferous carbonate platform overlain by 1-4 km of Mesozoic sediments; Grogan *et al.* 1999) and the ultra-deep East Barents Sea sedimentary basin in the east (Drachev *et al.* 2010) that stretches along the Novaya Zemlya islands (Fig. 1). The northern part of this basin is sometimes considered as a separate unit – North Barents Basin (e.g. Ivanova *et al.* 2011). The basin contains Upper Devonian to Cretaceous sediments with major subsidence during Permian-Triassic times (Drachev *et al.* 2010, Gac *et al.* 2012). Onshore western Franz Josef Land, a well penetrated a mainly Triassic section (including a thin layer of Carboniferous sediments) overlain by Barremian to Albian basalts interbedded with coal-bearing sediments (Dibner *et al.* 1992). The well penetrated an Vendian (Ediacaran) metamorphic basement at about ~2 km depth (Dibner *et al.* 1992). In the eastern part of the archipelago two wells were terminated at ~3.5 km in siliciclastic Middle Triassic (Anisian) strata. The stratigraphic interpretation of the seismic section in Fig. 3 generally follows Ivanova *et al.* (2011).

Dykes

As revealed by aeromagnetic data (Fig. 2), the dykes in the northern Barents Sea can be grouped in two regional swarms running oblique to the passive margin: the Franz Josef Land and Svalbard dyke swarms, respectively. The first swarm penetrates the existing structural grain of Franz Josef Land and the region north of Novaya Zemlya. In the west Svalbard region, the dykes could probably follow Caledonian (and older) faults (Ritzmann and Faleide 2007, Breivik *et al.* 2005, Gernigon & Brönner 2012). The Carboniferous grabens and associated faults (Faleide *et al.* 2008) could also facilitate magma migration at shallower levels south of Kong Karls Land (Minakov *et al.* 2012a). North of Kong Karls Land, the dykes cut pre-existing basement structures inferred from geophysical data. Most of dykes in Figs 1 & 2 are 30°- 90° off the boundaries of basement blocks and zones of weakness identified by Marello *et al.* (2013). We also notice that a number of dykes within the Svalbard swarm intersect each other. WNW-ESE

The northwest part of the Franz Josef Land archipelago is covered by plateau basalts that correspond to a broad magnetic high (Dibner 1998). The dykes intruding the sedimentary cover (and locally cutting the extrusive rocks) correlate with positive high-frequency and high-amplitude magnetic anomalies (see Supplementary figure S3 for additional data on the relationship between magmatic and sedimentary rocks). We assume that the dyke emplacement during a normal polarity period and a steep orientation of the natural remanent magnetization (Abashev *et al.* 2015) allows for this direct correlation.

In multichannel seismic data (Figs 4 & 5) the dykes can be identified as sub-vertical discontinuities that can be traced below 6-7 seconds (13 – 15 km depth) and pinching out at about 2 seconds (~ 3 km depth) as was also shown before by Khlebnikov *et al.* (2011). The sills in the East Barents Basin are often spatially associated with these vertical zones of disrupting seismic signatures. On seismic these vertical features are wider at the top crystalline basement and pinch out at the average depth of sills. The seismic horizons bend upwards in the vicinity of these anomalies that can be related to the ascending magma and/or fluids. The dyke anomalies are best imaged on the eastern flank of the East Barents Basin (southeast of Franz Josef Land). In the central part of the basin the interpretation is more complicated below the high velocity sill complex (described in detail in the following section and also by Polteau *et al.* 2016). Here the dyke anomalies are thinner and occur locally as we show a zoomed subset of the uninterpreted seismic section (Fig. 5). We acknowledge that the interpretation of these features is not unique. For example, a localized flow of metamorphic fluids, penetrating crystalline basement, could also result in a similar pattern.

Sills and lava flows

In MCS data (Figs 4 & 5) we identify sill intrusions resided in the East Barents Sea Basin using the following criteria: high (positive) acoustic impedance contrast, unconformable relations to host sedimentary layers, and saucer-shaped geometry of reflectors (Figs. 4, 5 and S3). In seismic sections, these sub-horizontal anomalies are most clearly observed in the Middle Triassic strata. Sub-volcanic intrusive and extrusive mafic rocks are also assumed in the lowermost Cretaceous strata based on MCS data. Similar magmatic rocks are observed within the Upper Jurassic Agardfjellet Formation in the Kong Karls Land platform (Grogan *et al.* 2000).

Most of the saucer-shaped sill intrusions visible on seismic data are within Triassic organic-rich siliciclastic rocks in the central part of the profile (Figs 4 & 5). A possible large sub-horizontal sill complex (lateral extent of 100-200 km) can be identified near the top basement at ~6 s or about 13-km depth (Figs 4 & 5). This interpretation is supported by two sills (150 and 400 m thick) in the Lower

Carboniferous and a thick mafic sill at the top basement (Carboniferous – Ediacaran transition) penetrated by a borehole in western Franz Josef Land (Fig. S3; Dibner 1998, p. 126).

The average thickness of sills observed onshore Franz Josef Land both in boreholes and outcrops varies in the range of 20-100 meters. A similar thickness of sills is reported for the Svalbard region (Senger *et al.* 2014a). The metamorphic aureoles are observed within a few tens of meters of the dyke contact in Franz Josef Land (Dibner *et al.* 1992). The thickness of contact aureoles in the host sediments reported for Spitsbergen is 1.5-2 times larger than the thickness of sills (Senger *et al.* 2014b).

Possible hydrothermal vent complexes are identified at about 1.5-1.8 seconds (1.5-2 km depth) in the eastern flank of the basin, just above the dyke anomalies (Fig. 5). A northerly location of the major volcanic activity is suggested by the presence of lava flows on Franz Josef Land (particularly abundant in the western part of the archipelago) and on Kong Karls Land (east of Svalbard). Sill intrusions in the north are generally shallower (and in younger stratigraphic intervals) compared to the southern part of the East Barents Basin (Shipilov & Karyakin 2011) possibly indicating a northward increase of magma volume and pressure.

Structure of crystalline crust

The crustal P-wave velocity model (Fig. 3) indicates that the northern part of the East Barents Sea Basin is confined between two higher-velocity domains (profile distance of 0-400 km and 750-1000 km, respectively). The thicker crust in the east is probably related to the northernmost tip of the Novaya Zemlya fold-and-thrust belt that links to the Taimyr foldbelt in the east (Drachev *et al.* 2010). The western part of the profile can be interpreted as a Caledonian crystalline basement modified by mafic intrusions (at the profile distance of 0-300 km). The northern East Barents Sea Basin is characterized by lower velocities of the crystalline crust (5.8-7.1 km/s). The Moho depth within the basin varies between 29 km and 35 km. It increases to the east and approaches of over 40 km at the northern tip of the Novaya Zemlya fold-and-thrust belt . A slight increase of crustal thickness east of Svalbard can be the result of mafic intrusions in the lower crust. The crustal thickening and/or buckling due to Eocene Eurekan/Svalbard Orogeny cannot be also excluded. At the same time, a number of observations suggest that the formation of the fold-and-thrust belt was associated with a thin-skin deformation restricted to western Svalbard (e.g. Leever *et al.* 2011). Thus, it appears from the lower crustal velocities that the amount of possible underplated intrusive material or magmatic lower crust is limited. In addition, the velocity model across the northern Barents Sea does not indicate significant stretching of the crust associated with the LIP magmatism assuming 35 km as an average thickness of the continental crust. The bulk velocities in the crystalline crust are in the range of 6.0-7.0 km/s, which is much lower than is typical for a mafic igneous lower crust (Ridley & Richards 2010). This indicates that the magma transport in the crust was rather localized than pervasive (underplating). Despite these two processes are generally not mutually exclusive, we conclude that most of the High Arctic LIP intrusions in the northern Barents Sea have been emplaced by a localized magma transport such as dyking and/or channelized magmatic flow.

The pattern of P-wave velocity anomalies (Fig. 3b) is characterized by the presence of high velocity finger-shaped anomalies that have been previously interpreted east of Svalbard as parts of a Lower Cretaceous magmatic feeder system (Minakov *et al.* 2012a). The high velocity anomalies south of Kong Karls Land (up to 10% with respect to 1D background velocity model) are spatially correlated with the sills and dykes at shallower levels. The dyke-like anomalies in the multichannel data in Figs 4 & 5 are sometimes spatially correlated with higher compressional velocities in the crystalline crust. A 2-3 km increase of the Moho depth is observed beneath this type of velocity anomalies in the western part of the profile (Fig. 3; 0-100 km).

The architecture of the crystalline crust is characterized by the basement highs and lows which correspond to gentle domes and sinks in the structure of the sediments above. The reflection seismic data indicate that the Franz Josef Land region represented a structural high already in Mesozoic times whereas Cenozoic uplift and erosion (Henriksen *et al.* 2011, Minakov *et al.* 2012b) emphasized the present-day topography in the northeast Barents Sea.

Conceptual model

We summarize the geological and geophysical information in the form of a conceptual model in Fig. 6. The model includes magmatic source region which forms at the brittle/plastic-viscous rheology transition, radiating dykes, and sills within the sedimentary basin. A radial stress pattern is exerted by the deep mantle plume. The lithosphere is weakened by melts and fluids above the magmatic source region. The magma may ascend vertically in porous melt-rich channels in the viscous regime (Connolly & Podladchikov 2007, Keller *et al.* 2013) and spread laterally (away from the source region) at the level of neutral buoyancy. The magma transport in the brittle-plastic part of the lithosphere occurs in dykes. Most of eruptions occur in the axial volcanic zone above the hot mantle plume. In the vicinity of the sedimentary basin the level of neutral buoyancy deepens due to the density decrease in sediments compared to the adjacent basement rocks. The sills are fed by dykes (mostly from below) and spread sideways at weak sedimentary horizons. This conceptual picture forms the basis for our mechanical model that aims to infer regional palaeo-stress field and associated geometry of dykes in the northern Barents Sea.

4 Mechanical models for dyke emplacement

Model geometry and problem setup

Mechanical modelling of deformation associated with a magmatic reservoir is an important tool towards better understanding of the emplacement process (see Grosfils *et al.* (2013) for elastic models and Gerbault (2012) for elastoplastic models). Specifically, the geometry of dykes in horizontal plane is often explained using 2D elastic mechanical models (Odé 1957, Muller & Pollard 1977, McKenzie *et al.* 1992, Hou *et al.* 2010). The setup of our mechanical model is inspired by these previous studies.

The model consists of an elastic (or elastoplastic) circular plate containing a circular hole and subject to a pressure and shear stress boundary conditions (Fig. 7a). The inner and outer radii are 200 km and 1200 km, respectively. We use a plane strain approximation that is assumed to be valid at mid-crustal depths. The deformation related to the vertical stresses is ignored. Thus, our model setup should be equivalent to an upper lithosphere weakened by a circular mantle plume. The effects of fluid/melt pressure, temperature and prescribed rules of strain softening are not included in our model. A more complete description of the problem would have to include a 3D visco-elasto-plastic thermomechanical model and multiphase physics. However, given the sparsity and uncertainty of the geological and geophysical data, we believe that our simplified model constitutes a reasonable first-order approach.

We further specify the inner boundary as a free surface that corresponds to a weak inner region. In our numerical experiments we explore the effect of far-field shear stress and corresponding stress concentration around the central circular region weaken by mantle plume. We start with isotropic boundary conditions, i.e. radial extension. Then, we proceed by introducing some amount of far-field pure shear.

Analytical solution for elastic rheology

Let us first consider an analytical solution to the mechanical problem of stress concentration around a circular inclusion assuming that all deformation is elastic. Yarushina and Podladchikov (2007) derived an analytical solution to a similar problem using the method of Muskhelishvili (1953). The model is subject to boundary conditions for homogeneous pressure ($\sigma_{rr} = p(t)$) and zero hoop stress ($\sigma_{r\theta} = 0$) at the inner boundary and the homogeneous horizontal stress components ($\sigma_{xx} = \sigma_{xx}^{\infty}(t)$, $\sigma_{yy} = \sigma_{yy}^{\infty}(t)$) and zero shear stress ($\sigma_{xy} = 0$) at the outer boundary. The solution for stresses is given by the following expressions:

$$\sigma_{rr} = p^{\infty} - \Delta P\left(R/r\right)^2 - \tau\left(1 - 4\left(R/r\right)^2 + 3\left(R/r\right)^4\right)\cos 2\theta; \quad (1)$$

$$\sigma_{\theta\theta} = p^{\infty} + \Delta P\left(R/r\right)^2 + \tau\left(1 + 3\left(R/r\right)^4\right)\cos 2\theta; \quad (2)$$

$$\sigma_{r\theta} = \tau\left(1 + 2\left(R/r\right)^2 - 3\left(R/r\right)^4\right)\sin 2\theta; \quad (3)$$

where $\sigma_{rr}, \sigma_{\theta\theta}, \sigma_{r\theta}$ are the radial hoop and shear stress components; (r, θ) are polar coordinates; R is the inner radius, p^{∞} is the pressure at the outer boundary, ΔP - pressure difference at the inner and outer radii, $\tau = \left(\sigma_{yy}^{\infty} - \sigma_{xx}^{\infty}\right)/2$ is the shear stress at the outer boundary. Here and everywhere else in the paper, we assume that the tensile stresses are positive. The solution in terms of the maximum shear stress $\tau_{\max} = \sqrt{\left(\sigma_{yy} - \sigma_{xx}\right)^2/4 + \sigma_{xy}^{\;2}}$ is presented for isotropic boundary conditions $\tau = 0$ (Fig. 8a) and for $\tau = \Delta P/2$ (Fig. 8b). The pressure gradient and far-field pressure (e.g. due to gravitational potential energy differences) is set to 10 MPa .

Geometry of tensile (mode-I) fractures

The seismic velocity model in Fig. 3 indicates no significant regional stretching of the crust. Therefore, we suggest that the deformation associated with magma emplacement in the northern Barents Sea was localized by brittle-plastic failure of the crust linked to the process of dyking. According to Anderson's criterion, once the dyke is initiated it propagates normal to the least principal stress (Anderson 1937; Pollard 1973; Delaney *et al.* 1986). Odé (1957) employed this idea to explain the radiating geometry of the Spanish Peaks dykes at the eastern edge of the Colorado Plateau. McKenzie *et al.* (1992) further developed this model to explain the geometry of dykes on Earth (Mackenzie dyke swarm in the Canadian Shield) and Venus (associated with coronae structures) by constructing stress trajectories for the direction normal to the least compressive stress. These studies used an analytical solution for a perforated elastic plate in a plane strain approximation similar to the one described before. However, these authors were mainly interested in the area far from the plume and made an assumption that $R/r \ll 1$, which implies that the radius of the circular hole is small compared to the distance from the centre of the hole. Alternatively, Hou *et al.* (2010) used a finite-element model of thin elastic plate with a large circular "plug" stressed at the external boundaries to model directions of principal stresses and matched the geometry of dykes within the Mackenzie swarm.

Following these authors, we derive the largest principal stress trajectories using the analytical elastic solution from equations (1) – (3) and solving numerically an ordinary differential equation:

$$\frac{dy}{dx} = tg\theta(x, y), \tag{4}$$

in which the angle $\theta(x, y)$ determines the orientation of principal stresses given that

$$\theta(x, y) = \frac{1}{2} arctg\left(\frac{2\sigma_{xy}(x, y)}{\sigma_{xx}(x, y) - \sigma_{yy}(x, y)} \right). \tag{5}$$

We use a 4th-order Runge-Kutta method to integrate equations (4) and (5).

Without shear applied, the geometry of tensile fractures is radially symmetric (Fig. 8a). Adding of the far-field shear component leads to deviation of trajectories from a radial trend towards the direction nearly orthogonal to the extension (Fig. 8b). Deviation occurs at distances nearly equal to the plume diameter. Close to the plume tensile stress still exhibits nearly radial pattern. These trajectories might represent the geometry of the dyke swarm if initiating fractures were not interacting with each other, i.e., were located at a considerable distance or were immediately healed after initiation by material with similar elastic properties.

To date this model provides the most popular explanation of the geometry of dykes in giant swarms. The model is elegant, easy to implement and gives required physical intuition based on the parameter $\tau / \Delta P$. This dependence can be slightly modified by the external pressure p^{∞}. The approach based on elastic model may give correct results for the case of a single fracture. However, each new fracture must modify the stress state and, thus, the next dyke should be modelled using a slightly different stress distribution.

Moreover, the geometry of dyke swarms suggests more complicated settings than predicted by the elastic model. The density of dyke populations across the stress trajectories is not uniform. There are some preferred emplacement directions. The curvature of dykes can be different compared to predictions. Dykes may swing and intersect each other.

Geophysical and geological observations provided in Figs. 1-2, and Fig. S3 suggest that dykes that apparently belong to the same LIP event can intersect and can be affected by each other and local crustal heterogeneity. We interpret some magnetic anomalies (Fig. 2 and Fig. S3) as fractures (or shear zones) oriented orthogonal to the main strike of the dyke planes. The existence of shear zones cutting dykes is documented on Franz Josef Land (Dibner 1998). Geological observations on many islands of the archipelago indicate that some mafic intrusions cut the lava flows and the Early Cretaceous sedimentary rocks (Dibner *et al.* 1992). These observations suggest that the dykes within the swarm intruded neither independently nor simultaneously. We believe that a more consistent formulation for the modelling of fracture networks such as dyke swarms should include irreversible plastic deformation. However, analytical solutions for this type of problems are complicated and exist only for small $\tau/\Delta P$. Thus, numerical solutions are required.

Numerical elastoplastic Model 1

The development of plastic deformation in the crust can be viewed either as formation and growth of microcracks or sliding on grain boundaries. The upper crust is considered to deform through cataclastic faulting while a semibrittle regime is more typical at higher pressures (Hirth & Tullis 1994). This behaviour is well described using the Mohr-Coulomb yield criterion

$$F = \tau_{\max} + \left(\frac{\sigma_{xx} + \sigma_{yy}}{2} \right) \sin\varphi - Y_s, \qquad (6)$$

where φ is the friction angle, Y_s is the yield stress, $\tau_{\max}$ is the maximum shear stress. In the elastoplastic models, the total strain rate can be decomposed on the elastic and plastic components as soon as yield criterion $F = 0$ is reached (Yu 2007). Elastic components are still governed by Hooke's law, while for plastic components plastic flow law is applied. This leads to additional dependence of elastoplastic stiffness tensor on stresses. The relationship between the strain rate and stress rate can be written as

$$\underline{\dot{\boldsymbol{\sigma}}} = \underline{\underline{\mathbf{D}}}^{ep} \cdot \underline{\dot{\mathbf{e}}}^{total}, \qquad (7)$$

where $\underline{\dot{\mathbf{e}}}^{total}$ is the total strain rate (written as a 3x1 vector for finite element numerical implementation); $\underline{\dot{\boldsymbol{\sigma}}}$ is the stress rate (3x1 vector); $\underline{\underline{\mathbf{D}}}^{ep}$ is a 3x3 elastoplastic tangent modular matrix that depends on elastic and plastic material parameters and stresses, namely:

$$\underline{\underline{\mathbf{D}}}^{ep} = \underline{\underline{\mathbf{D}}} \left(I - \frac{\partial Q}{\partial \underline{\boldsymbol{\sigma}}} \frac{\partial F}{\partial \underline{\boldsymbol{\sigma}}} \underline{\underline{\mathbf{D}}} \middle/ \frac{\partial F}{\partial \underline{\boldsymbol{\sigma}}} \underline{\underline{\mathbf{D}}} \frac{\partial Q}{\partial \underline{\boldsymbol{\sigma}}} \right) \qquad (8)$$

Implicit in this equation is that plastic deformation is governed by flow potential Q, which is usually taken in the form similar to the yield function

$$Q = \tau_{\max} + \left(\frac{\sigma_{xx} + \sigma_{yy}}{2} \right) \sin\psi + const. \qquad (8)$$

Here, ψ is the dilation angle that controls the volume increase during shear. We first consider the case of associated plastic flow. In the associative plasticity, the friction angle is equal to dilatation angle ($\psi = \varphi$), which means that shear on the fault plane is accompanied by a similar component of volume increase.

Our numerical elastoplastic model is based on the formulation and the MATLAB code by Yarushina *et al.* (2010). The stresses are integrated using finite element method (Zienkiewicz & Taylor 2005). We use a forward Euler incremental method for solving elastoplastic problems. The loading is incrementally increased towards the yield stress. The algorithm accounts for the drift from the yield surface and force equilibrium. The accuracy of the numerical solution is benchmarked versus elastic and elastoplastic analytical solutions by Yarushina *et al.* (2010).

The numerical grid consists of 1000x1000 elements with an adaptive cell size of 0.6 x 1.2 km close to the circular hole and 1.4 x 7.5 km at the outer boundary (Fig. 7a). We choose 4-node isoparametric quadrilateral elements. The dimensions of the model are the same as in the elastic case (inner and outer radii are 200 km and 1200 km, respectively). Boundary conditions are pressure and pure shear stress applied at the outer boundary. Both friction and dilation angles are set to 30^{o}. The yield stress in equation (6) is 30 MPa. The elastic parameters are: Poisson's ratio of 0.3 and shear modulus of 30 GPa. Note, that the elastic solution for stresses given in equations (1) – (3) is independent of material parameters. The initial pressure at the outer boundary is 10 MPa. The values of the yield function (Eq. 6) are shown for isotropic stress (radial extension) boundary conditions (Fig. 9a) and combined pressure-shear loading at $\tau = \Delta P / 2$ (Fig. 9b).

Geometry of shear (mode-II) fractures

A number of previous studies suggested that the zones of shear failure may serve as pathways for magma migration in the crust (Regenauer-Lieb 1998, Weinberg & Regenauer-Lieb 2010, Gerbault 2012). In these models, the direction of shear failure and faulting in the crust is predicted using a plane strain slip-line theory. This approach has been also applied in other geodynamic settings (Tapponnier & Molnar 1976, Regenauer-Lieb & Petit 1997). The two sets of conjugate shear trajectories (α- and β- slip-lines) are found from an equation similar to equation (4):

$$\frac{dy}{dx} = tg\left(\theta(x, y) \pm (\pi / 4 - \varphi / 2)\right). \tag{9}$$

The slip-lines represent the shear failure (mode-II fracture) pattern inside the plastic zone (Fig. 9). For purely isotropic load ($\sigma_{xx}^{\infty} = \sigma_{yy}^{\infty}$), the slip trajectories show a symmetric fan-shaped logarithmic spiral pattern (Fig. 9a). A similar pattern of crustal fractures was previously obtained by Gerya (2014) using a 3D numerical thermomechanical model of Venusian coronae structures. Applying of the shear load ($\sigma_{xx}^{\infty} \neq \sigma_{yy}^{\infty}$) results in the formation of two pairs of conjugate fault populations bisected by the largest compressive stress (vertical) direction (Fig. 9b). The curvature of the slip-lines depends on the friction angle. However, it does not significantly affect the general pattern. It should be noted that the way the trajectories are computed using equation (9) does not depend on the specific problem and this technique can be used in models with different geometry and boundary conditions.

Using the slip-line approach we can predict the arcuate geometry of dilatant faults (Fig. 9). The geometry of slip-lines shows preferred directions (not axisymmetric) when far-field shear is applied (Fig. 9b). The drawback of this approach is that the location and spacing of slip-lines is predefined by numerical grid and not by rock heterogeneity or any other physical factors. Moreover, the experiments on rock deformation show that the dilation angle should decrease with the increase of strain and must be smaller than the friction angle ($\psi < \varphi$). This leads to different kinematic and stress characteristics, implying that stress and strain will have localization along different directions. At the same time, laboratory experiments and field observation of borehole break-outs show that localization of strain and stress occurs within shear bands that may deviate from slip-lines (Vardoulakis *et al.* 1988; Papamichos *et al*. 2010).

Numerical elastoplastic Model 2 and shear bands

The numerical Model 2 is similar to Model 1 except that we use here a non-associative plastic flow law ($\psi < \varphi$). Thus, in this approach the yield function is different from the flow potential ($F \neq Q$). This type of rheology leads to instabilities of deformation and formation of shear bands (Rudnicki & Rice 1975). These are observed experimentally and have been modelled numerically (Cundall 1989). Dilational effects are very common in rocks during shear. This phenomenon is partly due to small asperities at the fault planes that dilate the fracture until the strain reaches some critical value (Vermeer & de Borst 1984). The critical yield stress can be higher in dilatant rocks since a part of the elastic energy can be spent on the volume change before the material breaks in shear. However, laboratory and *in situ* observations of rock deformation show that the dilation angle is much smaller than the friction angle and typically is around $\psi = 8$°, while the friction angle is typically around $\varphi = 30$° (Vermeer & de Borst 1984). The boundary conditions are the same as in Model 1 (Fig. 7). The development of plastic shear bands around a magma chamber was previously studied using numerical elastoplastic modelling by Gerbault (2012). The model proposed in this study can be viewed as a larger-scale implementation of the approach presented by this author.

Our numerical experiments show that initial (physical) heterogeneity is required for localization by shear-banding. Tests with homogeneous models and without shear applied did not show localization of deformation in shear bands. Small-scale heterogeneities are intrinsic to the crust as indicated by seismological studies of coda (scattered) waves associated with regional seismic phases (Sato *et al.* 2012). Thus, we impose an initial random isotropic field on the yield stress (shown in Fig. 7b). We use a Gaussian autocorrelation function to make a random realization. The maximum amplitude of heterogeneity is 2% and the correlation length is ~8 km.

The regime of isotropic extension (pressure boundary condition) results in a fan-shaped logarithmic spiral pattern of dilatant shear bands (Figs. 10a and 11a). The shear bands initiate at the inner boundary adjacent to the assumed mantle plume and propagate outward while the far-field pressure is incrementally increased (Figs. 10-11). The angle of shear bands with respect to the largest principal stress lies in the range of Coulomb ($\pi/4-\varphi/2$) to Arthur angle ($\pi/4-(\varphi+\psi)/4$) (Vermeer & de Borst 1984). Both the pressure (Fig. 10) and shear stress (Fig. 11) are reduced within the shear bands. Thus, the material softening in our model is not prescribed but results from formation of shear bands. The observed dilatation and weakening is favourable for focusing of fluid or magma inside the deformation bands since much lower fluid (magma) pressures are needed to overcome resistance from the rock. The shear bands turn beyond one diameter to the shear direction following the Coulomb angle when shear loading is applied (Figs 10b and 11b). The geometry of shear bands is bisected by the direction of the far-field largest compressive stress. The strain localization in our mechanical model is caused by the rheological instability and does not involve any prescribed weakening rule. The plastic shear strain and volumetric strain (dilatation) within shear bands are shown in Supplementary Figure S4.

Our results show that the mechanical model including the non-associated elastoplastic rheology is a suitable approach to describe the deformation around the plume centre. It captures the general pattern of the two conjugate dyke swarms in the northern Barents Sea (Figs. 1 and 2). The dilatant shear bands initiate on random (physical, not numerical) small-scale heterogeneities in the crust and propagate away from the magmatic centre. We propose that under-pressured weak shear bands facilitate magma transport in the vicinity of the source region. The propagation of the fractures further away from the magmatic centre is further addressed in the Discussion. For instance, the dykes may change the propagation regime from mode-II to mode-I fracture depending on a local state of stress.

5 Discussion

Palaeo-reconstruction of Amerasia Basin and geometry of dyke swarms

Pre-breakup reconstructions of the Amerasia Basins often juxtapose the East Siberian and Arctic Alaska margin with the Canadian Arctic margin for the Early Cretaceous epoch (Drachev & Saunders 2006, Drachev 2011, Grantz *et al.* 1998, Sweeney 1985, Lawver *et al.* 2002, Shephard *et al.* 2013). These kinematic models imply a counter-clockwise rotation of the Arctic Alaska plate at the spreading axis oriented nearly orthogonal to the northern Barents Sea margin. In this study we employ a similar pre-breakup kinematic reconstruction of the Amerasia Basin (Fig. 12a) that generally follows the model by Shephard *et al.* (2013). In addition, it includes the Chukchi Borderland and Bennett Island located north of Franz Josef Land (Drachev & Saunders 2006). It should be also noted that the relative position of the New Siberian Islands is not accurately restored in Fig. 12 due to Late Cretaceous – Cenozoic extension in the East Siberian shelf (Drachev *et al.* 2010, Drachev 2011). The position of Ellesmere and Axel Heiberg Island is modified due to Early Cenozoic compression and formation of the Eurekan fold-and-thrust belt (Piepjohn *et al.* 2007). In Fig. 12a, Ellesmere and Axel Heiberg Island are shifted towards Greenland compared to the model by Shephard *et al.* (2013). The light grey lines for Arctic Canada indicate the location of coastlines in the reconstruction by Shephard et al. (2013). This configuration creates geometrical problems to fit in the Lomonosov Ridge when the Eurasia Basin is closed. The previously published configuration of Ellesmere Island has been tentatively introduced to account for the Eurekan compression by fixing the northern coastline and extending the Ellesmere and Axel Heiberg islands to the south. However, the amount of compression and exact location of the blocks that composed the Ellesmere and Axel Heiberg islands are poorly constrained (G. Shephard pers. comm. 2016). In the presented reconstructions, we have moved the entire block by ~200 km to the south. This configuration provided a more reasonable configuration with respect to the closure of the Eurasia Basin.

Four areas of Early Cretaceous magmatism can be identified in the circum-Arctic region: the East Svalbard, Franz Josef Land, Arctic Canada, and the area adjacent to the Arctic Alaska margin and Bennett Island (Drachev & Saunders 2006, Tegner & Pease 2014). The geometry of dykes in the northern Barents Sea is proposed in this contribution (Figs. 1 & 2). The geometry of dykes in Arctic Canada (Fig. 12a) follows Buchan & Ernst (2006). The Canada dykes strike obliquely (30°-45°) with respect to the passive margin. The quadruple spatial distribution of magmatism forms a pattern that resembles the conjugate families of dilatant plastic shear bands obtained in our numerical experiments when a far-field shear stress was applied at the outer boundary (Figs. 10b, 11b & 12b). However, taking into account complexities of the local stress state and the younger deformation we do not attempt to match the exact geometry of dykes in the circum-Arctic region.

At the same time, we find that the general pattern of dykes in the northern Barents Sea (Fig. 12a) is well captured by geometry of dilatant shear bands in our model (Fig. 12b). This can be interpreted in terms of dyke emplacement controlled by conjugate shear directions away from a magmatic center north of the northern Barents Sea margin. We suggest that the network of dilatant shear bands served as pathways for magma and/or developed concurrent to the magma emplacement (see also further discussion on the problem of magma transport in the next section). Similarly, our model can explain the orientation of dykes in the Sverdrup Basin of Arctic Canada including Axel Heiberg Island and Ellesmere Island (Fig. 12a). However, the initial geometry of dykes in this region could be modified by younger deformation.

Based on existing laboratory experiments (Katz *et al.* 2003, Holtzman *et al.* 2006) and numerical models (Keller *et al.* 2013, Gerya *et al.* 2015, Gerya & Burov 2015) we anticipate that the magmatic weakening of the lithosphere, associated with the axial volcanic zone and magma-rich shear bands, should have evolved rapidly (within 1-2 Myr) through continental breakup to development of an oceanic spreading center where most of volcanic activity should occur. However, this model is complicated by observations of a younger Cretaceous volcanism on the Arctic Canada margin.

Recent U-Pb dating results on the timing of magmatism in Arctic Canada Islands were reported by Evenchik *et al.* (2015). These authors have analyzed samples from the Cretaceous dolerite sills and volcaniclastic rocks on Ellef Ringnes Island. The U-Pb dating of intrusive rocks gave ages of 120-126 Ma, similar to Corfu et al. (2013). The volcaniclastic rocks are younger (~101-105 Ma). This probably indicates a prolonged volcanic activity after the main intrusive event at 120-126 Ma. The volcanic activity could be associated with seafloor spreading center parallel to the Arctic Canada margin and formation of the Alpha Ridge volcanic plateau (e.g. Funck *et al.* 2011). The prolonged volcanism on the Arctic Canada margin is also indicated by the radioisotopic and geochemical analyses of silicic volcanic rocks on the northern coast of Ellesmere Island (~97-104 Ma) (Estrada *et al.* 2016). We can speculate that lithosphere rifting in a combination with small-scale mantle convection (e.g. model by Nielsen & Hopper 2004) could be responsible for this younger (post-breakup) volcanic activity on the rifted margin of Arctic Canada. In contrast, the Barents Sea margin was probably located farther away from the plume center and was separated by the Lomonosov Ridge microcontinent. This can explain the lack of younger Cretaceous volcanism on the Barents Sea margin.

The pre-breakup reconstruction of Greenland suggests that some dykes in northern Greenland could belong to the Svalbard swarm. However, recent U-Pb dating of several dykes in this region has shown much younger ages of ~80-85 Ma (Thorarinsson *et al.* 2015). Early Cretaceous basalts are also found in the Chukchi Borderland and Bennett Island (Drachev & Saunders 2006) but the resolution of magnetic data in this region is not high enough to identify dykes.

We propose that the High Arctic LIP dykes were initiated by utilizing a fracture pattern originating from a plume-related pressure gradients and regional far-field shear stresses in the continental lithosphere. The geometry of dykes in large swarms is shown to be controlled by regional principal stresses. Pre-existing heterogeneities in the crust can lead to local stress concentrations which might alter dyke geometry only locally not affecting the regional pattern. A combination of extension related to the opening of the Canada Basin and a smaller compressional component during the Early Cretaceous epoch can explain the mode of lithospheric failure and emplacement of mafic dyke swarms in the Arctic region (Fig. 12b). The direction of largest tensile stress follows the kinematic model for the opening of the Canada Basin that is sub-parallel to the northern Barents Sea margin. On the palaeo-Pacific side, some compression can be related to multiple terrain accretion along the Koyukuk-Nutesyn and Farallon subduction zones (Shephard *et al.* 2013).

Timing of breakup

The magmatic weakening of the proto-Arctic lithosphere associated with the LIP would subsequently lead to continental breakup and initiation of seafloor spreading in the Amerasia Basin shortly after 122-124 Ma. The assumption of earlier seafloor spreading in the Amerasia Basin, as suggested by Grantz *et al.* (2011) and in other publications would create a mechanical problem: the deformation must have been focused in the weakest region (i.e. at the mid-ocean ridge or plate boundary) while failure of adjacent thick continental crust and concurrent dyke emplacement would not have occurred.

Døssing *et al.* (2013) based on interpretation of new aeromagnetic data have suggested that the Franz Josef Land and Arctic Canada dyke swarms might also cross the Alpha Ridge and adjacent Lomonosov Ridge margin. The formation of the Alpha Ridge would definitely postdate the time of breakup. The seismic velocity structure of the Alpha Ridge indicates that the crustal thickness of this structure is about 30 km (Funck *et al.* 2011). About 2/3 of the crust has P-wave velocities >7.1 km/s suggesting a mafic igneous crystalline basement. Dredging and seismic reflection data indicate thick basaltic cover at shallower levels. We assume that even if some fragments of continental crust intruded by dykes were preserved below the basalts, these fragments must have been highly attenuated and deformed. In our opinion, the linear magnetic anomalies on the Alpha Ridge, mapped by Døssing *et al.* (2013), should be more likely related to structures of oceanic rifting with excess magmatism (similar to Iceland rift zones). The discrepancy of a large amount of extension in the Amerasia Basin and very little regional extension in the northern Barents Sea would require a mechanical decoupling of these two regions at a post-breakup time.

Another argument constraining the timing of continental breakup is the requirement of continental denudation area north of the Barents Sea margin during Barremian-Aptian time. The latter is suggested by Barremian-Aptian fluvial deposits in the Barents Sea and Svalbard linked to tectonic uplift in the north (Maher 2001, Midtkandal & Nystuen 2009). The river deltas were prograding into southerly regions during Barremian time (Smelror *et al.* 2009). The MCS data in the central Barents Sea show clinoforms prograding from the north and northeast source areas to the southern sink region (Dimitriou 2014, Midtkandal *et al.* 2015). The transition from mainly shale to the Barremian sandstone units is responsible for a regional stratigraphic horizon throughout the northern Barents Sea (Grogan *et al.* 1999). On Svalbard, the Helvetiafjellet Formation is associated with a change of paleoenvironment from marine to nearshore-continental containing coal layers and footprints of dinosaurs. The Isachsen Formation in the Sverdrup Basin of Arctic Canada and the Kuparuk Formation in north Alaska (Leith *et al.* 1992) can be considered as analogues to the Helvetiafjellet Formation and linked to the plume-related surface topography.

Magma transport within East Barents Sea Basin

Understanding the mechanism of magmatic intrusions into sedimentary basins has important implications for petroleum industry and paleoclimate research. Seismic data and borehole information obtained within the East Barents Sea Basin indicate the presence of a dolerite sill complex that seemingly extends throughout the entire basin (Shipilov & Karyakin 2011, Polteau *et al.* 2016; and Chapter 3 of this paper). At the same time, the eastern branch of the dyke swarm south of Franz Josef Land cuts the northern East Barents Basin nearly orthogonally (some dykes swing slightly towards the basin in the western part of the archipelago; Figs. 1-2). Below we discuss possible mechanisms controlling the magma transport in the continental crust away from the plume-related magmatic source region into the Barents Sea.

The zone of shear failure were suggested to facilitate magmatic transport away from an upper crustal magma chamber (Gerbault 2012), in a form of anastomosing dykes at deep crustal levels (Weinberg & Regenauer-Lieb 2010), and on lithospheric scales associated with Alpine collision (Regenauer-Lieb 1998). Localized melt bands oriented along shear directions have been observed in laboratory experiments on deformation of partially molten aggregates (Holtzman *et al.* 2003, Katz *et al.* 2006). White *et al.* (2011) reported on mainly double-couple earthquake mechanisms (mode-II fracture) associated with dyke propagation from mid-crustal depths in Iceland. Laboratory experiments on quartz aggregates by Hirth & Tullis (1994) indicate a transition from dominant mode-I to dominant mode-II microfracturing that occurs at about 0.6 GPa. In nature the depth of this transition is probably also controlled by temperature and composition. Thus, the dilatant plastic shear bands may facilitate the magma migration where the mode-I fractures are inhibited by higher confining pressure, temperature and other reasons.

Lateral propagation of magma in dykes is assumed to be driven by magma pressure at the source region and topographic gradients (Fialko & Rubin 1999). Theoretical models (e.g. Lister & Kerr 1991) predict the lateral propagation of dykes in the crust along the level of neutral buoyancy. The effect of the topographic gradient (or more generally, gravitational potential energy difference) on the dyke propagation path has been recently illustrated by monitoring the growth of a 45-km long dyke in Iceland (Sigmundsson *et al.* 2015). Both theory and observations suggest that a laterally spreading dyke can propagate into an area with falling lithostatic pressure while the depth of propagation is controlled by the level of neutral buoyancy. The lithostatic pressure at given depth and the depth to the level of neutral buoyancy must have been deeper in the sedimentary basin when compared to Franz Josef Land. Thus, it may partly explain the reorientation of magma flow towards the East Barents Sea Basin.

The extent of vertical versus horizontal magma transport mechanism in the lithosphere cannot be ruled out. The study of anisotropic magnetic susceptibility of the Mackenzie dyke swarm by Ernst & Baragar (1992) suggests that the flow within dykes is mostly vertical within ~500-km horizontal distance from the magmatic centre and mostly horizontal farther away. Taking this as a first-order estimate, the magma transport within the East Barents Sea Basin might have occurred through the lateral flow at the level of neutral buoyancy.

The surface topography as another controlling parameter at the time of emplacement can be inferred based on structural and lithological constraints. Grogan *et al.* (2000) interpreted north-northwest trending flexures at the Mesozoic level within the Kong Karls Land platform in multichannel seismic data. The flexure developed above the Late Paleozoic faults reactivated in Late Mesozoic and Cenozoic times. The field relations indicate that flood basalts in Kong Karls Land were extruded on top of a nearly flat landscape. Following their arguments, the flexure was filled-in by the lowermost part of fluvial sediments of the Helvetiafjellet Formation before the eruption. These observations indicate that the elevated topography north of the Barents Sea margin initiated before the eruption of flood basalts in Kong Karls Land.

Another prominent topographic feature in the Barents Sea region is the NNE-SSW oriented Novaya Zemlya foldbelt. This foldbelt follows the eastern flank of the East Barents Basin and was probably formed in Triassic-earliest Jurassic times (Drachev *et al.* 2010). Paleogeographic reconstructions for the Cretaceous period indicate that Novaya Zemlya was a highland region (Smelror *et al.* 2009). Thus, this elevated topography could affect the stress regime and propagation path of dykes. The faults and zones of weakness associated with this fold belt could also provide the zones of increased permeability. In addition to that, the distribution of gravitational potential energy in the Barents Sea could lead to rotation of principal stresses from horizontal to vertical planes. This would change the preferred mode of magma emplacement from dykes to sills. Poro-elastoplastic numerical models by Rozhko et al. (2007) suggest that fluid-filled fractures pressurized from below tend to develop as vertical dykes or V-shaped intrusions in horizontal extension while sub-horizontal intrusions develop in a compressive stress regime. Thus, the compression associated with surface topography changes could contribute to the formation of the thick sill complex in the East Barents Sea Basin. A geological analogue to the East Barents Sea intrusive complex is the dolerite intrusions along the deformation front of the Transantarctic Mountains associated with the Ferrar LIP (Elliot et al. 1999). Ernst *et al.* (1995) provided other geological examples of sedimentary basins intruded by sills that were fed by dyke swarms.

Porous flow localized by a channeling instability (Connolly & Podladchikov 2007; Yarushina *et al.*, 2015) is another mechanism of magma transport as an alternative to fluid filled fractures. Such fluid flow initiates in response to the fluid overpressure and propagate in the direction of the pressure gradients. Formation of dyke-like features by the mechanism of shear fractures explained above may be accompanied by such processes. This model could probably explain kilometres-scale thickness of vertical column-like anomalies observed in the seismic reflection images and tomographic velocity models (Figs. 3 - 5). The next step toward understanding the magma transport in dykes and sills should be implementation of two-phase viscoelastoplastic deformation models such as presented by Keller *et al.* (2013) and Yarushina *et al.* (2015). The effect of three-dimensional stress field should also be taken into account.

6 Conclusions

Geophysical and geological data in the Barents Sea indicate that an area in excess of 1.5 x 10^6 km^2 has been affected by the Early Cretaceous volcanism. The northern Barents Sea was affected by two dolerite dyke swarms: in the eastern Svalbard and Franz Josef Land regions, respectively. Multichannel seismic data indicate that the dykes fed the dolerite sills, resided in Permian to Early Cretaceous sedimentary strata in the northern Barents Sea. In multichannel seismic data the dyke-like anomalies penetrate the entire sedimentary cover. Wide-angle seismic data indicate that the dykes or feeder channels may extend to mid-crustal depths (15-20 km) and possibly deeper. The Moho depth below the igneous province of 30-37 km is evidence that significant lithosphere thinning and decompressional melting did not occur. Seismic velocities in the lower crust do not exceed 7.1

km/s, indicating a lack of underplating. We infer a localized mode for both the deformation and magmatic transport within the crust.

These observations can be explained by magma transport in dykes radiating from a hot-spot region north of the Barents Sea margin shortly before the Amerasia Basin continental breakup. In support of this idea we considered a 2D plane strain elastoplastic finite-element modelling. The geometry of dykes in the northern Barents Sea region is predicted by the pattern of dilatant plastic shear bands in a model containing a circular hole with the radius of 200 km and subject to combined far-field extension pressure and pure shear load. Dilatant plastic shear bands are suggested to control the magmatic transport in the northern Barents Sea. Other mechanical models for formation of dyke swarms are discussed and their strengths and shortcomings are highlighted. We suggest that the far-field shear stress in the Early Cretaceous epoch resulted from a combination of extension in the Amerasia Basin subparallel to the northern Barents Sea margin and orthogonal compression related to palaeo-Pacific subduction.

Acknowledgements

A. Minakov acknowledges support from VISTA, project number 6264 and the Research Council of Norway through its Centres of Excellence funding scheme, project number 223272. We also thank Anna Mironova for helping to make Figure 6.

References:

Abashev, V., Mikhaltsov, N., & Vernikovsky, V. (2015). Paleomagnetism of Jurassic-Cretaceous basalts from the Franz Josef Land Archipelago: tectonic implications. In *EGU General Assembly Conference Abstracts* (Vol. 17, p. 797).

Anderson, E. M. (1937). IX.—The dynamics of the formation of cone-sheets, ring-dykes, and caldron-subsidences. *Proceedings of the Royal Society of Edinburgh*, *56*, 128-157.

Bailey, J. C., & Rasmussen, M. H. (1997). Petrochemistry of Jurassic and Cretaceous tholeiites from Kong Karls Land, Svalbard, and their relation to Mesozoic magmatism in the Arctic. *Polar Research*, *16*(1), 37-62.

Becker, J. J., D. T. Sandwell, W. H. F. Smith, J. Braud, B. Binder, J. Depner, D. Fabre, J. Factor, S. Ingalls, S-H. Kim, R. Ladner, K. Marks, S. Nelson, A. Pharaoh, G. Sharman, R. Trimmer, J. vonRosenburg, G. Wallace, P. Weatherall., Global Bathymetry and Elevation Data at 30 Arc Seconds Resolution: SRTM30_PLUS, Marine Geodesy, 32:4, 355-371, 2009.

Breivik, A. J., Mjelde, R., Grogan, P., Shimamura, H., Murai, Y., & Nishimura, Y. (2005). Caledonide development offshore–onshore Svalbard based on ocean bottom seismometer, conventional seismic, and potential field data. *Tectonophysics*, *401*(1), 79-117.

Buchan, K.L., & Ernst, R. (2006). Giant dyke swarms and the reconstruction of the Canadian Arctic islands, Greenland, Svalbard and Franz Josef Land. In *Dyke swarms — time markers of crustal evolution*. Edited by E. Hanski, S. Mertanen, T. Rämö, and J. Vuollo. Taylor and Francis/Balkema, London, UK., 27–48.

Buck, W. R. (2006). The role of magma in the development of the Afro-Arabian Rift System. *Geological Society, London, Special Publications*, *259*(1), 43-54.

Buiter, S. J., & Torsvik, T. H. (2014). A review of Wilson Cycle plate margins: A role for mantle plumes in continental break-up along sutures?. *Gondwana Research*, *26*(2), 627-653.

Coffin, M. F., & Eldholm, O. (1994). Large igneous provinces: crustal structure, dimensions, and external consequences. *Reviews of Geophysics*, *32*(1), 1-36.

Connolly, J. A. D., & Podladchikov, Y. Y. (2007). Decompaction weakening and channeling instability in ductile porous media: Implications for asthenospheric melt segregation. *Journal of Geophysical Research: Solid Earth*, *112*(B10).

Corfu, F., Polteau, S., Planke, S., Faleide, J. I., Svensen, H., Zayoncheck, A., & Stolbov, N. (2013). U–Pb geochronology of Cretaceous magmatism on Svalbard and Franz Josef Land, Barents Sea Large Igneous Province. *Geological Magazine*, *150*(06), 1127-1135.

Cundall, P. A. (1989). Numerical experiments on localization in frictional materials. *Ingenieur-archiv*, *59*(2), 148-159.

Delaney, P. T., Pollard, D. D., Ziony, J. I., & McKee, E. H. (1986). Field relations between dikes and joints: emplacement processes and paleostress analysis. *Journal of Geophysical Research: Solid Earth*, *91*(B5), 4920-4938.

Dimitriou, M. (2014). Lower Cretaceous Prograding Units in the eastern part of the SW Barents Sea. *Master Thesis*, University of Oslo.

Dibner, V. D. (1998). *Geology of Franz Josef Land*, Norsk Polarinstitutt, Oslo

Dibner, V., Bro, E., Pchelina, T., Preobrajenskaja, E. & Shkola, I. (1992). Geology of the Franz Josef Land archipelago, Russian Federation. In *Int Conf Arct Marg (ICAM 1992), ICAM Proceedings, Anchorage, Alaska* (Vol. 13).

Drachev, S., & Saunders, A. (2006). The Early Cretaceous Arctic LIP: its geodynamic setting and implications for Canada Basin opening. In *Proceedings of the Int. Conf. Arct. Margins, 4th, Anchorage* (pp. 216-223).

Drachev, S. S., Malyshev, N. A., & Nikishin, A. M. (2010). Tectonic history and petroleum geology of the Russian Arctic Shelves: an overview. In *Geological society, London, petroleum geology conference series* (Vol. 7, pp. 591-619). Geological Society of London.

Drachev, S. S. (2011). Tectonic setting, structure and petroleum geology of the Siberian Arctic offshore sedimentary basins. *Geological Society, London, Memoirs*, *35*(1), 369-394.

Døssing, A., Jackson, H. R., Matzka, J., Einarsson, I., Rasmussen, T. M., Olesen, A. V., & Brozena, J. M. (2013). On the origin of the Amerasia Basin and the High Arctic Large Igneous Province—results of new aeromagnetic data. *Earth and Planetary Science Letters*, *363*, 219-230.

Ebinger, C. J., & Casey, M. (2001). Continental breakup in magmatic provinces: An Ethiopian example. *Geology*, *29*(6), 527-530.

Eldholm, O., & Grue, K. (1994). North Atlantic volcanic margins: dimensions and production rates. *Journal of Geophysical Research: Solid Earth*, *99*(B2), 2955-2968.

Elliot, D. H., Fleming, T. H., Kyle, P. R., & Foland, K. A. (1999). Long-distance transport of magmas in the Jurassic Ferrar large igneous province, Antarctica. *Earth and Planetary Science Letters*, *167*(1), 89-104.

Ernst, R. E. (2014). *Large igneous provinces*. Cambridge University Press.

Ernst, R. E., & Baragar, W. R. A. (1992). Evidence from magnetic fabric for the flow pattern of magma in the Mackenzie giant radiating dyke swarm, *Nature*.

Ernst, R. E., Bleeker, W., Söderlund, U., & Kerr, A. C. (2013). Large Igneous Provinces and supercontinents: Toward completing the plate tectonic revolution. *Lithos*, *174*, 1-14.

Ernst, R. E., Head, J. W., Parfitt, E., Grosfils, E., & Wilson, L. (1995). Giant radiating dyke swarms on Earth and Venus. *Earth-Science Reviews*, *39*(1), 1-58.

Estrada, S., Damaske, D., Henjes-Kunst, F., Schreckenberger, B., Oakey, G. N., Piepjohn, K., & Linnemann, U. (2016). Multistage Cretaceous magmatism in the northern coastal region of Ellesmere Island and its relation to the formation of Alpha Ridge–evidence from aeromagnetic, geochemical and geochronological data. *NORWEGIAN JOURNAL OF GEOLOGY*, *96*(2), 65-95.

Evenchick, C. A., Davis, W. J., Bédard, J. H., Hayward, N., & Friedman, R. M. (2015). Evidence for protracted High Arctic large igneous province magmatism in the central Sverdrup Basin from stratigraphy, geochronology, and paleodepths of saucer-shaped sills. *Geological Society of America Bulletin*, B31190-1.

Faleide, J. I., Tsikalas, F., Breivik, A. J., Mjelde, R., Ritzmann, O., Engen, O., ... & Eldholm, O. (2008). Structure and evolution of the continental margin off Norway and the Barents Sea. *Episodes*, *31*(1), 82-91.

Farra, V., & Madariaga, R. (1987). Seismic waveform modeling in heterogeneous media by ray perturbation theory. *J. geophys. Res*, *92*(2697-2712), 140-146.

Fialko, Y. A., & Rubin, A. M. (1999). Thermal and mechanical aspects of magma emplacement in giant dike swarms. *Journal of Geophysical Research: Solid Earth*, *104*(B10), 23033-23049.

Funck, T., Jackson, H. R., & Shimeld, J. (2011). The crustal structure of the Alpha Ridge at the transition to the Canadian Polar Margin: Results from a seismic refraction experiment. *Journal of Geophysical Research: Solid Earth*, *116*(B12).

Gac, S., Huismans, R. S., Podladchikov, Y. Y., & Faleide, J. I. (2012). On the origin of the ultradeep East Barents Sea basin. *Journal of Geophysical Research: Solid Earth*, *117*(B4).

Gaina, C., Werner, S. C., Saltus, R., & Maus, S. (2011). Circum-Arctic mapping project: new magnetic and gravity anomaly maps of the Arctic. *Geological Society, London, Memoirs*, *35*(1), 39-48.

Gerbault, M. (2012). Pressure conditions for shear and tensile failure around a circular magma chamber; insight from elasto-plastic modelling. *Geological Society, London, Special Publications*, *367*(1), 111-130.

Gernigon, L., & Brönner, M. (2012). Late Palaeozoic architecture and evolution of the southwestern Barents Sea: insights from a new generation of aeromagnetic data. *Journal of the Geological Society*, *169*(4), 449-459. Gerya, T., & Burov, E. (2015). Formation and stability of ridge-ridge-ridge triple junctions in rheologically realistic lithosphere model. In *EGU General Assembly Conference Abstracts* , 17, 15090.

Gerya, T. V., Stern, R. J., Baes, M., Sobolev, S. V., & Whattam, S. A. (2015). Plate tectonics on the Earth triggered by plume-induced subduction initiation. *Nature*, 527(7577), 221-225.

Gerya, T. V. (2014). Plume-induced crustal convection: 3D thermomechanical model and implications for the origin of novae and coronae on Venus. *Earth and Planetary Science Letters*, *391*, 183-192.

Glebovsky, V. Y., Likhachev, A. A., Minakov, A. N., Poselov, V. A., Brekke, H., Ingen, Ø, & Faleide, J. I. (2006a). Regional distribution of sedimentary cover in the Nansen Basin based on magnetic data. *Geological and geophysical characteristics of the lithosphere of the Arctic region, St Petersburg, VNIIOkeangeologia*, 2006. Vol. 6. p. 188-193. (in Russian)

Glebovsky, V. Y., Kaminsky, V. D., Minakov, A. N., Merkur'ev, S. A., Childers, V. A., & Brozena, J. M. (2006b). Formation of the Eurasia Basin in the Arctic Ocean as inferred from geohistorical analysis of the anomalous magnetic field. *Geotectonics*, *40*(4), 263-281.

Grantz, A., Clark, D. L., Phillips, R. L., Srivastava, S. P., Blome, C. D., Gray, L. B., ... & Mickey, M. B. (1998). Phanerozoic stratigraphy of Northwind Ridge, magnetic anomalies in the Canada basin, and the geometry and timing of rifting in the Amerasia basin, Arctic Ocean. *Geological Society of America Bulletin*, *110*(6), 801-820.

Grantz, A., Hart, P. E., & Childers, V. A. (2011). Geology and tectonic development of the Amerasia and Canada Basins, Arctic Ocean. *Geological Society, London, Memoirs*, *35*(1), 771-799.

Grogan, P., Nyberg, K., Fotland, B., Myklebust, R., Dahlgren, S., & Riis, F. (2000). Cretaceous magmatism south and east of Svalbard: evidence from seismic reflection and magnetic data. *Polarforschung*, *68*, 25-34.

Grogan, P., Østvedt-Ghazi, A. M., Larssen, G. B., Fotland, B., Nyberg, K., Dahlgren, S., & Eidvin, T. (1999). Structural elements and petroleum geology of the Norwegian sector of the northern Barents Sea. In *Geological Society, London, Petroleum Geology Conference series* (Vol. 5, pp. 247-259). Geological Society of London.

Grosfils, E. B., McGovern, P. J., Gregg, P. M., Galgana, G. A., Hurwitz, D. M., Long, S. M., & Chestler, S. R. (2013). Elastic models of magma reservoir mechanics: a key tool for investigating planetary volcanism. *Geological Society, London, Special Publications*, *401*(1), 239-267.

Hames, W. E., Renne, P. R., & Ruppel, C. (2000). New evidence for geologically instantaneous emplacement of earliest Jurassic Central Atlantic magmatic province basalts on the North American margin. *Geology*, *28*(9), 859-862.

Henriksen, E., Bjørnseth, H.M., Hals, T.K., Heide, T., Kiryukhina, T., Kløvjan, O.S., Larssen, G.B., Ryseth, A.E., Rønning, K., Sollid, K. and Stoupakova, A. (2011). Uplift and erosion of the greater Barents Sea: impact on prospectivity and petroleum systems. *Geological Society, London, Memoirs*, *35*(1), pp.271-281.

Hirth, G., & Tullis, J. (1994). The brittle-plastic transition in experimentally deformed quartz aggregates. *Journal of Geophysical Research: Solid Earth*, *99*(B6), 11731-11747.

Hobro, J., & Singh, S. (1999). Joint interface and velocity estimation in three dimensions. *LITHOS Science Report*, *1*, 11-20.

Hobro, J. W., Singh, S. C., & Minshull, T. A. (2003). Three-dimensional tomographic inversion of combined reflection and refraction seismic traveltime data. *Geophysical Journal International*, *152*(1), 79-93.

Holtzman, B. K., Groebner, N. J., Zimmerman, M. E., Ginsberg, S. B., & Kohlstedt, D. L. (2003). Stress-driven melt segregation in partially molten rocks. *Geochemistry, Geophysics, Geosystems*, *4*(5).

Hou, G., Kusky, T. M., Wang, C., & Wang, Y. (2010). Mechanics of the giant radiating Mackenzie dyke swarm: a paleostress field modeling. *Journal of Geophysical Research: Solid Earth*, *115*(B2).

Ivanova, N. M., Sakulina, T. S., Belyaev, I. V., Matveev, Y. I., & Roslov, Y. V. (2011). Depth model of the Barents and Kara seas according to geophysical surveys results. *Geological Society, London, Memoirs*, *35*(1), 209-221.

Jakobsson, M., L. A. Mayer, B. Coakley, J. A. Dowdeswell, S. Forbes, B. Fridman, H. Hodnesdal, R. Noormets, R. Pedersen, M. Rebesco, H.-W. Schenke, Y. Zarayskaya A, D. Accettella, A. Armstrong, R. M. Anderson, P. Bienhoff, A. Camerlenghi, I. Church, M. Edwards, J. V. Gardner, J. K. Hall, B. Hell, O. B. Hestvik, Y. Kristoffersen, C. Marcussen, R. Mohammad, D. Mosher, S. V. Nghiem, M. T. Pedrosa, P. G. Travaglini, and P. Weatherall (2012). The International Bathymetric Chart of the Arctic Ocean (IBCAO) Version 3.0, Geophysical Research Letters, doi: 10.1029/2012GL052219.

Jerram, D. A., & Widdowson, M. (2005). The anatomy of Continental Flood Basalt Provinces: geological constraints on the processes and products of flood volcanism. *Lithos*, *79*(3), 385-405.

Katz, R. F., Spiegelman, M., & Holtzman, B. (2006). The dynamics of melt and shear localization in partially molten aggregates. *Nature*, 442(7103), 676-679.

Keller, T., May, D. A., & Kaus, B. J. (2013). Numerical modelling of magma dynamics coupled to tectonic deformation of lithosphere and crust. *Geophysical Journal International*, *195*(3), 1406-1442.

Kendall, J. M., Stuart, G. W., Ebinger, C. J., Bastow, I. D., & Keir, D. (2005). Magma-assisted rifting in Ethiopia. *Nature*, *433*(7022), 146-148.

Khlebnikov, P. A., Belenky, V. Y., Peshkova, I. N., Kazanin, G. S., Shkarubo, S. I., Pavlov, S. P., & Shlykova, V. V. (2011). Geological structure and petroleum potential of the eastern flank of the Northern Barents Basin. *Geological Society, London, Memoirs*, *35*(1), 261-269.

Klitzke, P., Faleide, J. I., Scheck-Wenderoth, M., & Sippel, J. (2015). A lithosphere-scale structural model of the Barents Sea and Kara Sea region. *Solid Earth*, *6*(1), 153.

Lawver, L. A., & Müller, R. D. (1994). Iceland hotspot track. *Geology*, *22*(4), 311-314.

Lawver, L. A., Grantz, A., & Gahagan, L. M. (2002). Plate kinematic evolution of the present Arctic region since the Ordovician. *Special Papers-Geological Society of America*, 333-358.

Leever, K.A.. Gabrielsen, R.H., Faleide, J.I. & Braathen, A. (2011). A transpressional origin for the West Spitsbergen ford-and-thrust belt: Insight from analog modeling. *Tectonics* 30, TC2014, doi:10.1029/2010TC002753.

Leith, T. L., Weiss, H. M., Mørk, A., Århus, N., Elvebakk, G., Embry, A. F., ... & Verba, M. L. (1992). Mesozoic hydrocarbon source-rocks of the Arctic region. *Arctic Geology and Petroleum Potential, Norw. Petrol. Soc. Spec. Publ*, *2*, 1-25.

Lister, J. R., & Kerr, R. C. (1991). Fluid-mechanical models of crack propagation and their application to magma transport in dykes. *Journal of Geophysical Research: Solid Earth*, *96*(B6), 10049-10077.

Maher Jr, H. D. (2001). Manifestations of the Cretaceous high Arctic large igneous province in Svalbard. *The Journal of Geology*, *109*(1), 91-104.

Marello, L., Ebbing, J., & Gernigon, L. (2013). Basement inhomogeneities and crustal setting in the Barents Sea from a combined 3D gravity and magnetic model. *Geophysical Journal International*, doi: 10.1093/gji/ggt018.

McKenzie, D., McKenzie, J. M., & Saunders, R. S. (1992). Dike emplacement on Venus and on Earth. *Journal of Geophysical Research: Planets*, *97*(E10), 15977-15990.

McHone, J. G., Anderson, D. L., Beutel, E. K., & Fialko, Y. A. (2005). Giant dikes, rifts, flood basalts, and plate tectonics: A contention of mantle models. *Geological Society of America Special Papers*, *388*, 401-420.

Midtkandal, I., & Nystuen, J. P. (2009). Depositional architecture of a low-gradient ramp shelf in an epicontinental sea: the lower Cretaceous of Svalbard. *Basin Research*, *21*(5), 655-675.

Midtkandal, I., Faleide, J. I., Planke, S., Dimitriou, M., Dahlberg, M., Myklebust, R., Nystuen, J. P., & Trosvik, T. H. (2015) Source-to-sink dynamics in the Early Cretaceous Boreal Basin; progradational lobes from a missing source, Geophysical Research Abstracts, AGU Fall Meeting, San Francisco.

Minakov, A., Mjelde, R., Faleide, J. I., Flueh, E. R., Dannowski, A., & Keers, H. (2012a). Mafic intrusions east of Svalbard imaged by active-source seismic tomography. *Tectonophysics*, *518*, 106-118.

Minakov, A., Faleide, J. I., Glebovsky, V. Y., & Mjelde, R. (2012b). Structure and evolution of the northern Barents-Kara Sea continental margin from integrated analysis of potential fields, bathymetry and sparse seismic data. *Geophysical Journal International*, *188*(1), 79-102.

Minshull, T. A., Lane, C. I., Collier, J. S., & Whitmarsh, R. B. (2008). The relationship between rifting and magmatism in the northeastern Arabian Sea. *Nature Geoscience*, *1*(7), 463-467.

Muller, O. H. & Pollard, D. D. (1977). The stress state near Spanish Peaks, Colorado determined from a dike pattern. *Pure and Applied Geophysics*, *115*(1-2), 69-86.

Muskhelishvili, N. I. (1953). Some basic problems of the mathematical theory of elasticity, Groningen, Holland.

Nejbert, K., Krajewski, K. P., Dubińska, E., & Pécskay, Z. (2011). Dolerites of Svalbard, north-west Barents Sea Shelf: age, tectonic setting and significance for geotectonic interpretation of the High-Arctic Large Igneous Province. *Polar Research*, 30.

Nielsen, T. K., & Hopper, J. R. (2004). From rift to drift: Mantle melting during continental breakup. *Geochemistry, Geophysics, Geosystems*, *5*(7).

Ntaflos, T., & Richter, W. (2003). Geochemical constraints on the origin of the continental flood basalt magmatism in Franz Josef Land, Arctic Russia. *European journal of mineralogy*, *15*(4), 649-663.

Odé, H. (1957). Mechanical analysis of the dike pattern of the Spanish Peaks area, Colorado. *Geological Society of America Bulletin*, *68*(5), 567-576.

Olesen, O., Brönner, M., Ebbing, J., Gellein, J., Gernigon, L., Koziel, J., ... & Solheim, D. (2010). New aeromagnetic and gravity compilations from Norway and adjacent areas: methods and applications. In *Geological Society, London, Petroleum Geology Conference series* (Vol. 7, pp. 559-586). Geological Society of London.

Paige, C. C., & Saunders, M. A. (1982). LSQR: An algorithm for sparse linear equations and sparse least squares. *ACM Transactions on Mathematical Software (TOMS)*, *8*(1), 43-71.

Papamichos, E., Tronvoll, J., Skjærstein, A., & Unander, T. E. (2010) Hole stability of red Wildmoor sandstone under anisotropic stresses and sand production criterion. *Journal of Petroleum Science and Engineering*, *72*, 78-92.

Piepjohn, K., Gosen, W. V., Estrada, S., & Tessensohn, F. (2007). Deciphering superimposed Ellesmerian and Eurekan deformation, Piper Pass area, northern Ellesmere Island (Nunavut). *Canadian Journal of Earth Sciences*, *44*(10), 1439-1452.

Piskarev, A. L., Heunemann, C., Makar'ev, A. A., Makar'eva, A. M., Bachtadse, V., & Aleksyutin, M. (2009). Magnetic parameters and variations in the composition of igneous rocks of the Franz Josef Land archipelago. *Izvestiya, Physics of the Solid Earth*, *45*(2), 150-166.

Pollard, D. D. (1973). Derivation and evaluation of a mechanical model for sheet intrusions. *Tectonophysics*, *19*(3), 233-269.

Polteau, S., Hendriks, B. W., Planke, S., Ganerød, M., Corfu, F., Faleide, J. I., ... & Myklebust, R. (2016). The Early Cretaceous Barents Sea Sill Complex: Distribution, 40 Ar/39 Ar geochronology, and implications for carbon gas formation. *Palaeogeography, Palaeoclimatology, Palaeoecology*, *441*, 83-95.

Regenauer-Lieb, K., & Petit, J. P. (1997). Cutting of the European continental lithosphere: plasticity theory applied to the present Alpine collision. *JOURNAL OF GEOPHYSICAL RESEARCH, 102*, 7731-7746.

Regenauer-Lieb, K. (1998). Dilatant plasticity applied to Alpine collision: ductile void growth in the intraplate area beneath the Eifel volcanic field. *Journal of Geodynamics*, *27*(1), 1-21.

Richards, M. A., Duncan, R. A., & Courtillot, V. E. (1989). Flood basalts and hot-spot tracks: plume heads and tails. *Science*, *246*(4926), 103-107.

Ridley, V. A., & Richards, M. A. (2010). Deep crustal structure beneath large igneous provinces and the petrologic evolution of flood basalts. *Geochemistry, Geophysics, Geosystems*, *11*(9).

Ritzmann, O., & Faleide, J. I. (2007). Caledonian basement of the western Barents Sea. *Tectonics*, *26*(5).

Rozhko, A. Y., Podladchikov, Y. Y., & Renard, F. (2007). Failure patterns caused by localized rise in pore-fluid overpressure and effective strength of rocks. *Geophysical Research Letters*, *34*(22).

Rudnicki, J. W., & Rice, J. R. (1975). Conditions for the localization of deformation in pressure-sensitive dilatant materials. *Journal of the Mechanics and Physics of Solids*, *23*(6), 371-394.

Sakoulina, T. S., Pavlenkova, G. A., & Kashubin, S. N. (2015). Structure of the Earth's crust in the northern part of the Barents–Kara region along the 4-AR DSS profile. *Russian Geology and Geophysics*, *56*(11), 1622-1633.

Sato, H., Fehler, M. C., & Maeda, T. (2012). *Seismic wave propagation and scattering in the heterogeneous earth* (Vol. 496). Berlin: Springer.

Smith, W. H. F., & Sandwell, D. T. (1997). Global seafloor topography from satellite altimetry and ship depth soundings, *Science*, 277, 1957-1962.

Senger, K., Tveranger, J., Ogata, K., Braathen, A., & Planke, S. (2014a). Late Mesozoic magmatism in Svalbard: A review. *Earth-Science Reviews*, *139*, 123-144.

Senger, K., Planke, S., Polteau, S., Ogata, K., & Svensen, H. (2014b). Sill emplacement and contact metamorphism in a siliciclastic reservoir on Svalbard, Arctic Norway. *NORWEGIAN JOURNAL OF GEOLOGY*, *94*(2-3), 155-169.

Shephard, G. E., Müller, R. D., & Seton, M. (2013). The tectonic evolution of the Arctic since Pangea breakup: Integrating constraints from surface geology and geophysics with mantle structure. *Earth-Science Reviews*, *124*, 148-183.

Shipilov, E. V., & Karyakin, Y. V. (2011). The Barents Sea magmatic province: Geological-geophysical evidence and new 40Ar/39Ar dates. In *Doklady Earth Sciences*, Vol. 439, No. 1, pp. 955-960.

Sigmundsson, F., Hooper, A., Hreinsdóttir, S., Vogfjörd, K.S., Ófeigsson, B.G., Heimisson, E.R., Dumont, S., Parks, M., Spaans, K., Gudmundsson, G.B. and Drouin, V. (2015). Segmented lateral dyke growth in a rifting event at Bárðarbunga volcanic system, Iceland. *Nature*, *517*(7533), pp.191-195.

Skilbrei, J. R. (1991). Interpretation of depth to the magnetic basement in the northern Barents Sea (south of Svalbard). *Tectonophysics*, *200*(1), 127-141.

Skilbrei, J. R. (1992). Preliminary interpretation of aeromagnetic data from Spitsbergen, Svalbard Archipelago (76–79 N): Implications for structure of the basement. *Marine Geology*, *106*(1), 53-68.

Smelror, M., Petrov, O. V., Larssen, G. B., & Werner, S. C. (2009). Geological history of the Barents Sea. *Norges Geol. undersøkelse*, 1-135.

Sweeney, J. F. (1985). Comments about the age of the Canada Basin. *Tectonophysics*, *114*(1), 1-10.

Svensen, H., Corfu, F., Polteau, S., Hammer, Ø., & Planke, S. (2012). Rapid magma emplacement in the Karoo large igneous province. *Earth and Planetary Science Letters*, 325, 1-9.

Tapponnier, P., & Molnar, P. (1976). Slip-line field theory and large-scale continental tectonics. *Nature*, *264*(5584), 319-324.

Tarduno, J. A. (1998). The high Arctic large igneous province. In *Third International Conference on Arctic Margins (*ICAM-III*)*, Celle, Germany.

Tegner, C., & Pease, V. (2014). Continental Flood Basalts of Bennett Island, East Siberian Sea: High Arctic Geodynamics. *EGU General Assembly Conference Abstracts*, 16, 2452.

Tegner, C., Storey, M., Holm, P. M., Thorarinsson, S. B., Zhao, X., Lo, C. H., & Knudsen, M. F. (2011). Magmatism and Eurekan deformation in the High Arctic Large Igneous Province: 40 Ar–39 Ar age of Kap Washington Group volcanics, North Greenland. *Earth and Planetary Science Letters*, *303*(3), 203-214.

Thórarinsson, S. B., Söderlund, U., Døssing, A., Holm, P. M., Ernst, R. E., & Tegner, C. (2015). Rift magmatism on the Eurasia basin margin: U–Pb baddeleyite ages of alkaline dyke swarms in North Greenland. *Journal of the Geological Society*, *172*(6), 721-726.

Verba, V. V., Astafurova, E. G., Leonov, V. O., Mandrikov, V. S., Chlupin, N. I. (2004). Structure of the Northern continental margin of the Barents Sea Shelf (in environments of Franz Joseph Land), *Geological-geophysical features of the lithosphere of the Arctic Region*, St. Petersburg, VNIIOkeangeologia, 5.

Vardoulakis, I., Sulem, J., & Guenot, A. (1988). Borehole instabilities as bifurcation phenomena. In *International Journal of Rock Mechanics and Mining Sciences & Geomechanics Abstracts* (Vol. 25, No. 3, pp. 159-170). Pergamon.

Vermeer, P. A., & De Borst, R. (1984). Non-associated plasticity for soils, concrete and rock. *HERON, 29 (3), 1984*.

Weinberg, R. F., & Regenauer-Lieb, K. (2010). Ductile fractures and magma migration from source. *Geology*, *38*(4), 363-366.

White, R. S., & McKenzie, D. (1995). Mantle plumes and flood basalts. *Journal of Geophysical Research: Solid Earth*, *100*(B9), 17543-17585.

White, R. S., Drew, J., Martens, H. R., Key, J., Soosalu, H., & Jakobsdóttir, S. S. (2011). Dynamics of dyke intrusion in the mid-crust of Iceland. *Earth and Planetary Science Letters*, *304*(3), 300-312.

Yarushina, V. M., & Podladchikov, Y. Y. (2007). The effect of nonhydrostaticity on elastoplastic compaction and decompaction. *Izvestiya, Physics of the Solid Earth*, *43*(1), 67-74.

Yarushina, V. M., Dabrowski, M., & Podladchikov, Y. Y. (2010). An analytical benchmark with combined pressure and shear loading for elastoplastic numerical models. *Geochemistry, Geophysics, Geosystems*, *11*(8).

Yarushina, V. M., Podladchikov, Y. Y., & Connolly, J. A. (2015). (De)compaction of porous viscoelastoplastic media: Solitary porosity waves. *Journal of Geophysical Research: Solid Earth*, *120*(7), 4843-4862.

Yu, H. S. (2007). *Plasticity and geotechnics* (Vol. 13). Springer Science & Business Media.

Zienkiewicz, O. C., & Taylor, R. L. (2005). *The finite element method for solid and structural mechanics*. Butterworth-heinemann.

Figure captions:

Figure 1. Bathymetry of the Barents Sea region. Red lines are axes of magnetic anomalies interpreted as Early Cretaceous dolerite dykes. A composite seismic transect (SVA – 4AR) crosses the giant radiating dyke swarms in the northern Barents Sea. The East Barents Sea basin is shown using contours of depth to top crystalline basement from Klitzke *et al.* (2015). KKL – Kong Karls Land. The location of the crustal-scale transect in Fig. 3 is shown by yellow line. The location of the seismic profile in Fig. 4 is shown by hatched grey line. The SRTM15_PLUS (release of 2015) global topography grid (Becker *et al.* 2009, Smith & Sandwell 1997) is used that includes the IBCAO bathymetry (Jakobsson *et al.* 2012) for the Arctic region.

Figure 2. Magnetic anomalies of the Barents Sea region. A composite seismic transect (SVA – 4AR) crosses the giant radiating dyke swarms in the northern Barents Sea. The East Barents Sea basin is shown using contours of depth to top crystalline basement from Klitzke *et al.* (2015). The higher resolution grids with a cell size of 2 km are highlighted in more saturated colours. KKL – Kong Karls Land. The location of the crustal-scale transect in Fig. 3 is shown by yellow line. The location of the seismic profile in Fig. 4 is shown by hatched grey line.

Figure 3. P-wave velocity model along the wide-angle profiles ESVA and 4AR. (A) The magnetic anomalies extracted along the crustal transect. (B) Results of refraction and reflection tomography in this study. Location of ocean bottom stations is shown by black triangles. (C) Results of forward modelling by Sakoulina *et al.* (2015). The velocity models do not show underplating, indicating predominantly localized (dykes, channelized magma flow) rather than pervasive magmatic transport associated with the High Arctic LIP in the northern Barents Sea. We suggest that most of crustal extension was taken up by brittle-plastic dilatation in shear bands.

Figure 4. Multichannel seismic data across the northern East Barents Basin, Profile 4-AR (380 - 850 km). See Fig. 1-2 for location. The interpretation of seismic stratigraphic unit follows Ivanova *et al.* (2011). The interpreted stratigraphic units are: K (green) – Cretaceous; J (blue) – Jurassic; T (magenta) – Triassic; P (brown) - Permian. Possible dykes/feeders and sills are highlighted with red colour. A number of sills are identified in Triassic strata; some sills are also inferred at deeper levels – in particular, at the sediment-crystalline basement interface. Most dyke-like anomalies are pinching out in Triassic strata. The location of the data subset shown in Fig. 5 is indicated by dashed box.

Figure 5. Zoomed uninterpreted multichannel seismic section showing mafic intrusive complexes within the northern East Barents Sea Basin.

Figure 6. Geofantasy on dyke emplacement and crustal structure within a continental large igneous province. Buoyancy-driven channelized magmatic flow originates in the lowermost lithosphere where a hot mantle plume stalls. In the brittle-plastic upper lithosphere the magma flow is focused in dykes radiating from the focal region weakened by ascending melts and fluids. The dykes propagate at the level of neutral buoyancy in the crust and feed sills in the sedimentary basin.

Figure 7. General setup of analytical and numerical models. The model is in horizontal plane. (A) The finite element mesh of the circular domain. The actual number of elements in the finite-element model is hundred times larger than shown in the figure. Thick arrows show the boundary constraints applied along the perimeter of the model. R – is the radius of circular hole in the centre of the model (200 km); σ_x^∞, σ_y^∞ are stresses at the outer radius; $p^\infty = (\sigma_x^\infty + \sigma_y^\infty)/2$ is pressure at the outer boundary. (B) The random Gaussian field of the yield strength used in the setup of numerical models. Correlation length is 8 km.

Figure 8. Elastic analytical solutions for the maximum shear stress. Trajectories of the largest principal stress are shown in white for pressure (A) and combined pressure and shear stress (pure shear) boundary conditions (B). These trajectories illustrate a possible geometry of tensile (mode-I) fractures in the crust. Red arrows indicate direction of external loading. Notice that the centre area has higher stresses. Therefore, fractures will be initiated from the centre.

Figure 9. Results of elastoplastic finite-element Model 1 (associated plasticity). Mohr-Coulomb yield stress (see Eq. 6) for isotropic extension (pressure) boundary conditions (A) and combined pressure and shear stress (pure shear) boundary conditions: $\tau = -\Delta P / 2$, (B). Slip lines illustrate a possible geometry of shear (mode-II) fractures in the crust.

Figure 10. Results of elastoplastic finite-element Model 2 (non-associated plasticity). The pressure field is shown for isotropic extension (pressure) boundary conditions (A) and combined pressure and shear stress (pure shear) boundary conditions: $\tau = -\Delta P / 2$, (B). Thick arrows show the boundary constraints applied along the perimeter of the model. The extension pressure is positive. Note that most shear bands are under-pressured (i.e. dilating).

Figure 11. Results of elastoplastic finite-element Model 2 (non-associated plasticity). The maximum shear stress field is shown for isotropic extension (pressure) boundary conditions (A) and combined pressure and shear stress (pure shear) boundary conditions: $\tau = -\Delta P / 2$, (B). Thick arrows show the boundary constraints applied along the perimeter of the model. Note low shear stress inside shear bands.

Figure 12. Geometry of the High Arctic LIP dyke swarms. (A) Mafic dykes on top of the plate kinematic reconstruction for the Arctic region at ~140 Ma. The kinematic model follows Shephard *et al.* (2013). In this study, Ellesmere and Axel Heiberg Island are moved towards Greenland by ~200 km to account for the early Cenozoic Eurekan orogeny. The configuration of the in the model by Shephard *et al.* (2013) is also shown using thinner lines. (B) The maximum (plastic) shear strain computed for combined pressure and pure shear stress boundary conditions ($\tau = -\Delta P / 2$). The plastic strain is localized within shear bands. Geometry of dykes in Arctic Canada follows Buchan & Ernst (2006). EL – Ellesmere, AX – Axel Heiberg Island, SV – Svalbard, FJL – Franz Josef Land, KKL – Kong Karls Land, BI - Bennett Island, CHB – Chukchi Borderland, AAM – Artic Alaska margin, GRE – Greenland, AR – Alpha Ridge and tentative location of magmatic centre. Thin grey lines show isobath -1600 m.

Tables:

Table 1. Acquisition parameters of the multichannel seismic reflection data

Table 2. Specifications of aeromagnetic data

Supplementary figures:

Fig. S3. Relationship between magmatic and sedimentary rocks in Franz Josef Land. Schematic geological transect modified from Dibner *et al.* (1992) (upper plate) and the grid of high-resolution aeromagnetic data (lower plate). Zoomed map of magnetic anomalies in Fig. 2 for the Franz Josef Land region is shown. The legend for the geological transect: 1- Cenozoic sediments, 2- Undifferentiated Triassic-Jurassic sedimentary rocks, 3 – Basaltic lava flows, 4 – Dolerite dykes. The magnetic anomalies derived from a grid are shown above the geological transect. The triangles along the transect show the location of boreholes.

Fig. S4. Results of elastoplastic finite-element Model 2 (non-associated plasticity). The maximum shear stress field is shown in MPa. Combined pressure and pure shear stress boundary conditions ($\tau = -\Delta P / 2$). (A) Maximum plastic shear strain (B) Bulk plastic strain (dilatation). Positive sign indicates volume increase.

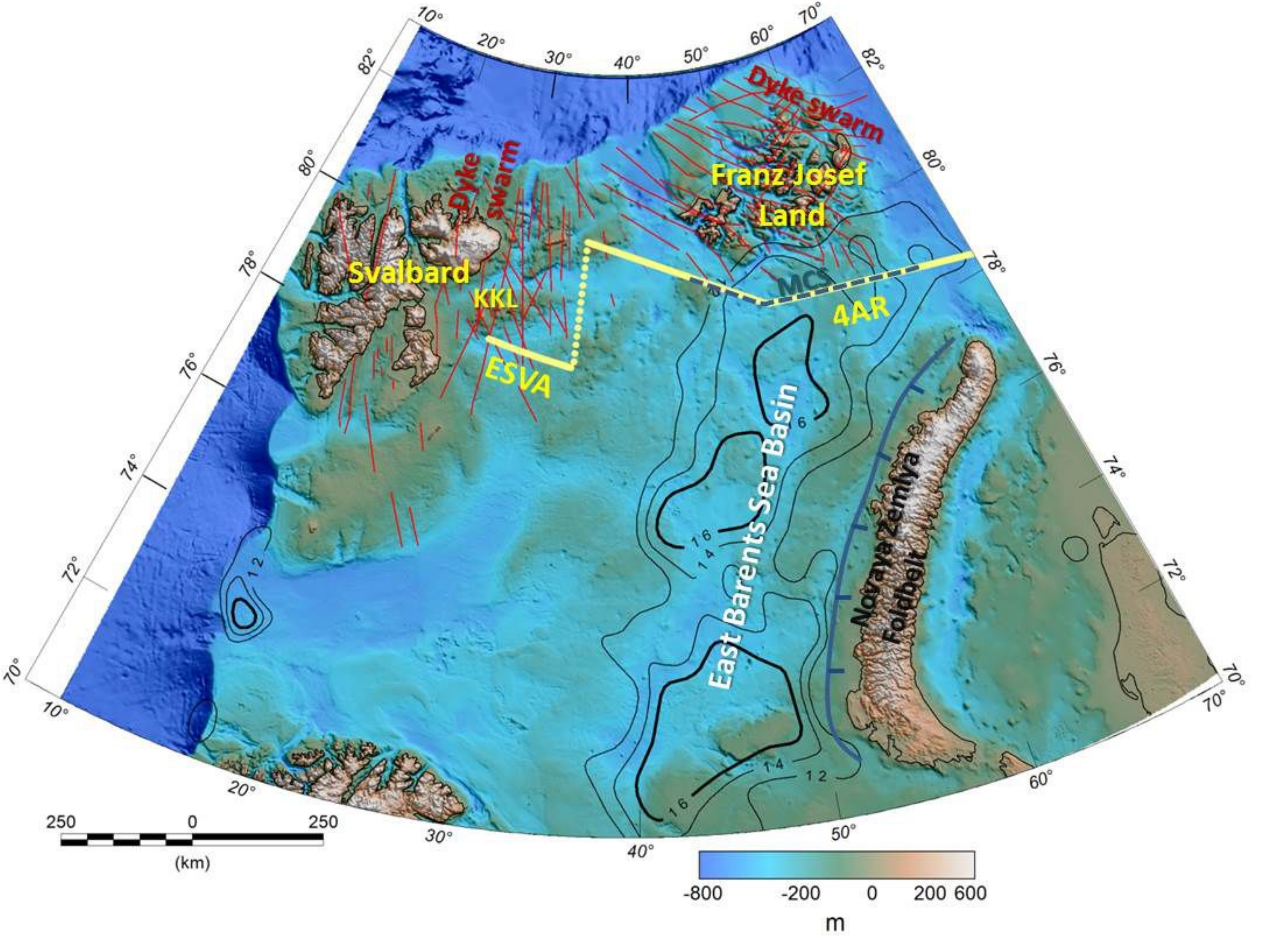

Dyke swarm
Dyke swarm
Franz Josef Land
Svalbard
KKL
ESVA
MCS
4AR
East Barents Sea Basin
Novaya Zemlya Foldbelt
16
14
12
6
250
0
250
(km)
-800
-200
0
200
600
m
10°
20°
30°
40°
50°
60°
70°
70°
72°
74°
76°
78°
80°
82°

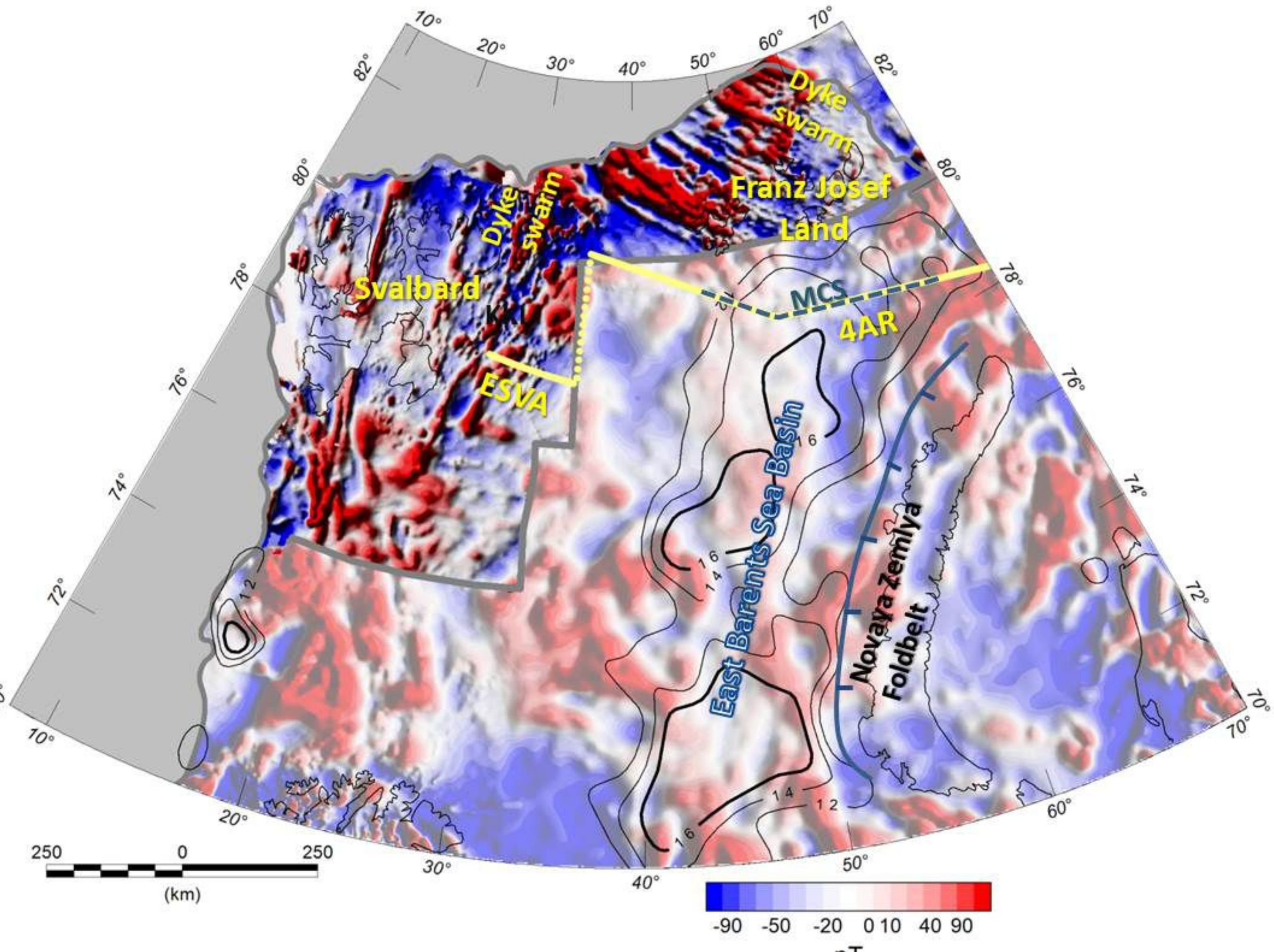

Dyke swarm
Franz Josef Land
Dyke swarm
Svalbard
KKL
ESVA
MCS
4AR
East Barents Sea Basin
Novaya Zemlya Foldbelt
250
0
250
(km)
-90
-50
-20
0
10
40
90
nT

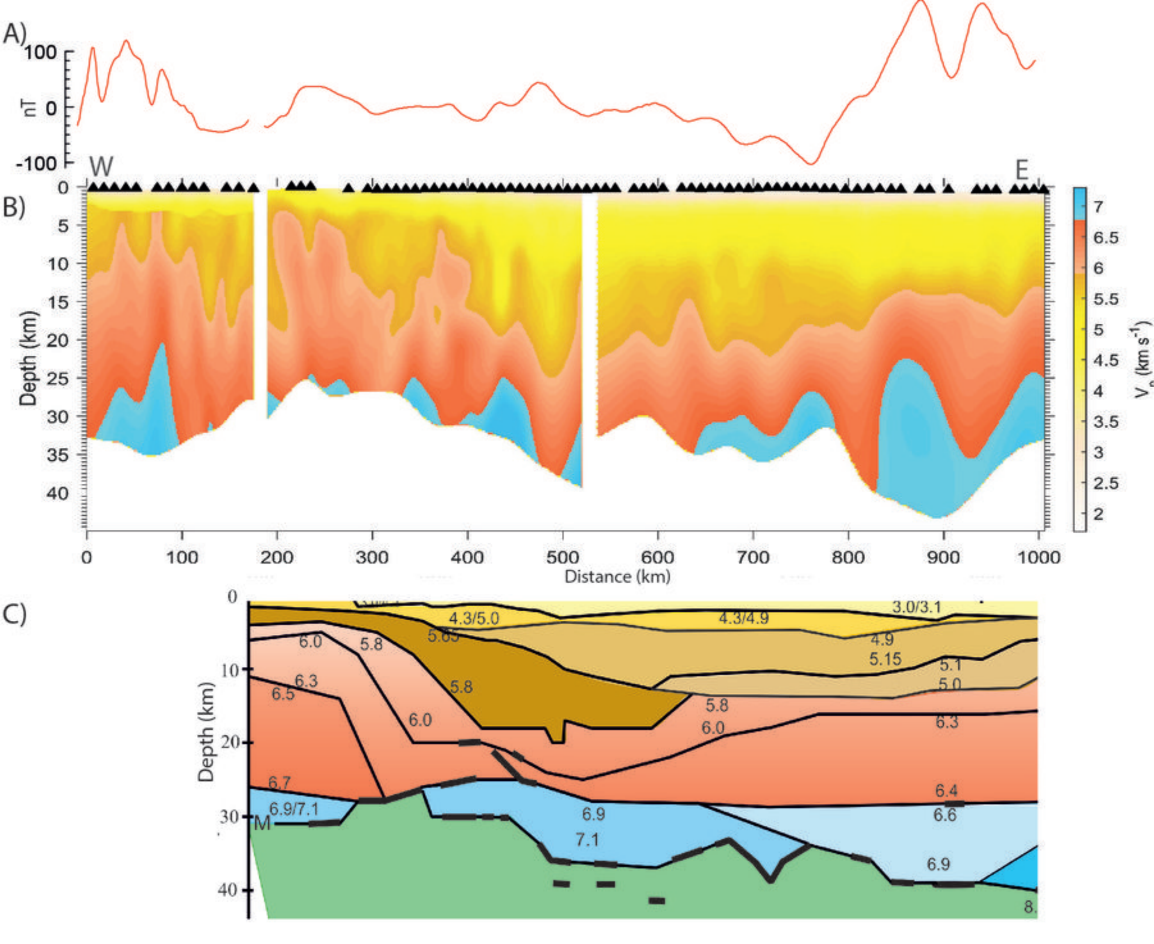
A)
B)
C)
nT
W
E
Depth (km)
Distance (km)
V_p (km s^{-1})
4.3/5.0
4.3/4.9
3.0/3.1
4.9
5.15
5.1
5.0
5.65
5.8
6.0
6.3
6.5
6.7
6.9/7.1
M
6.9
7.1
6.4
6.6
8.

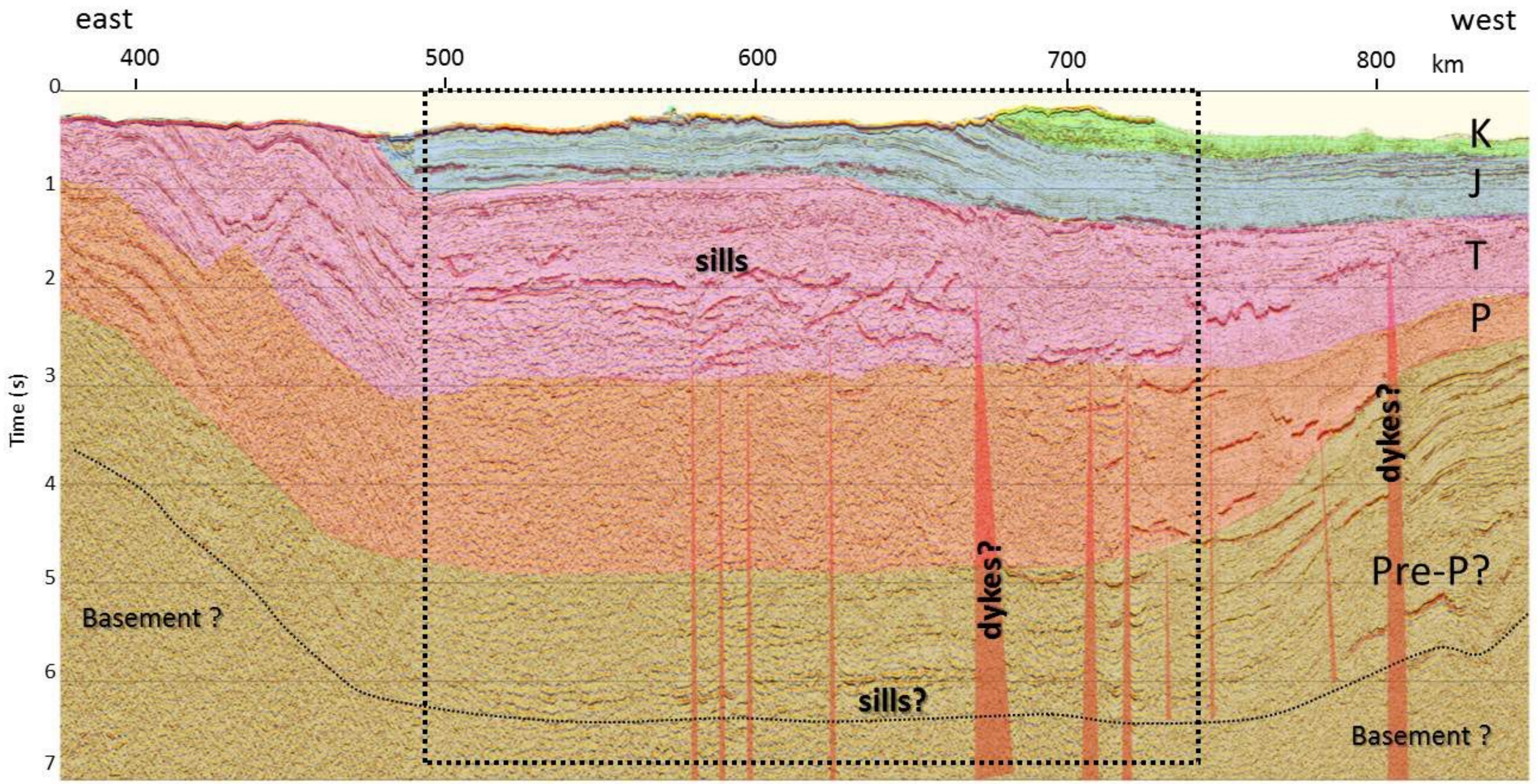
east
west
400
500
600
700
800
km
0
1
2
3
4
5
6
7
Time (s)
K
J
T
P
Pre-P?
sills
sills?
dykes?
dykes?
Basement ?
Basement ?

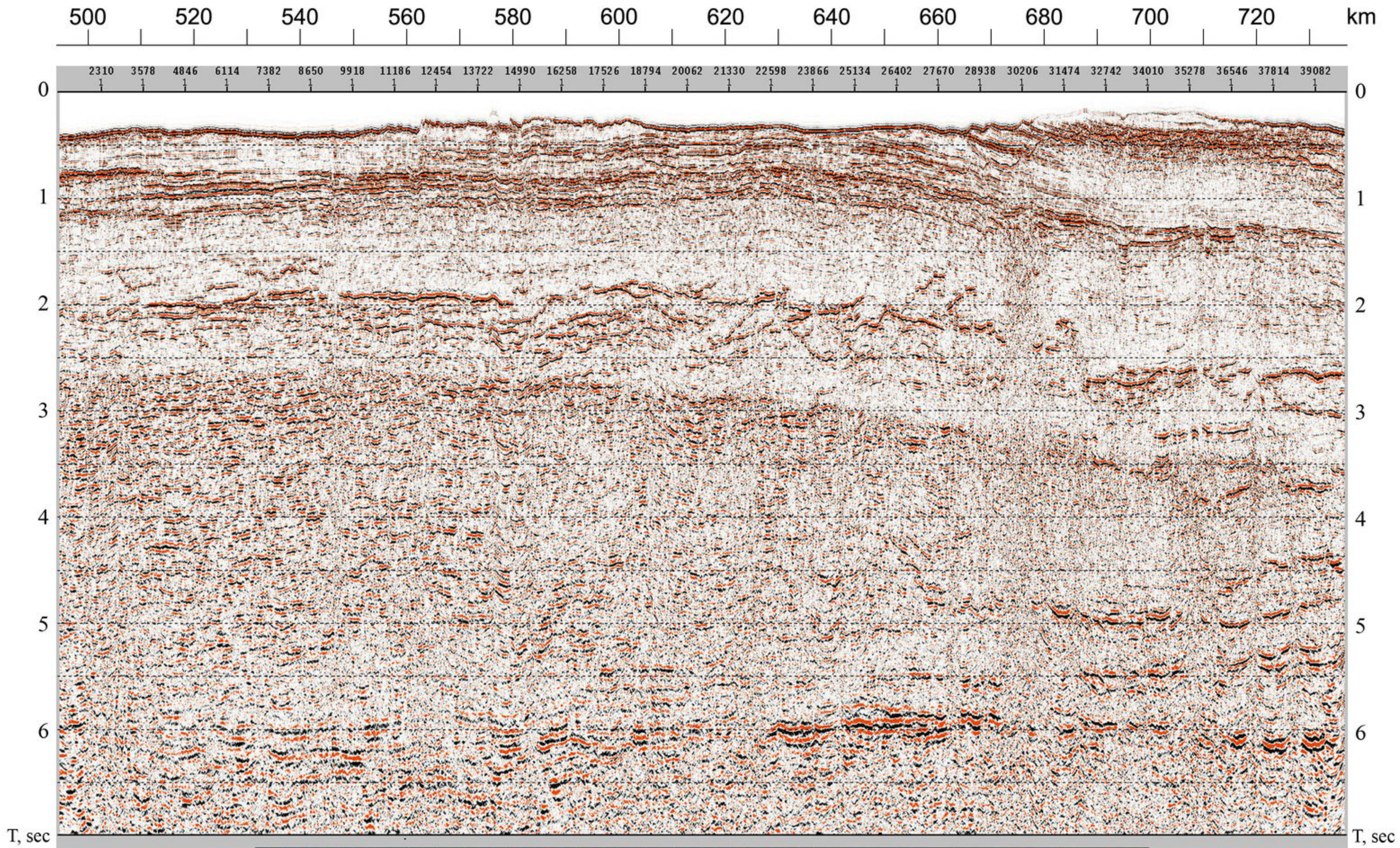

km
500
520
540
560
580
600
620
640
660
680
700
720
2310 3578 4846 6114 7382 8650 9918 11186 12454 13722 14990 16258 17526 18794 20062 21330 22598 23866 25134 26402 27670 28938 30206 31474 32742 34010 35278 36546 37814 39082
0
1
2
3
4
5
6
T, sec

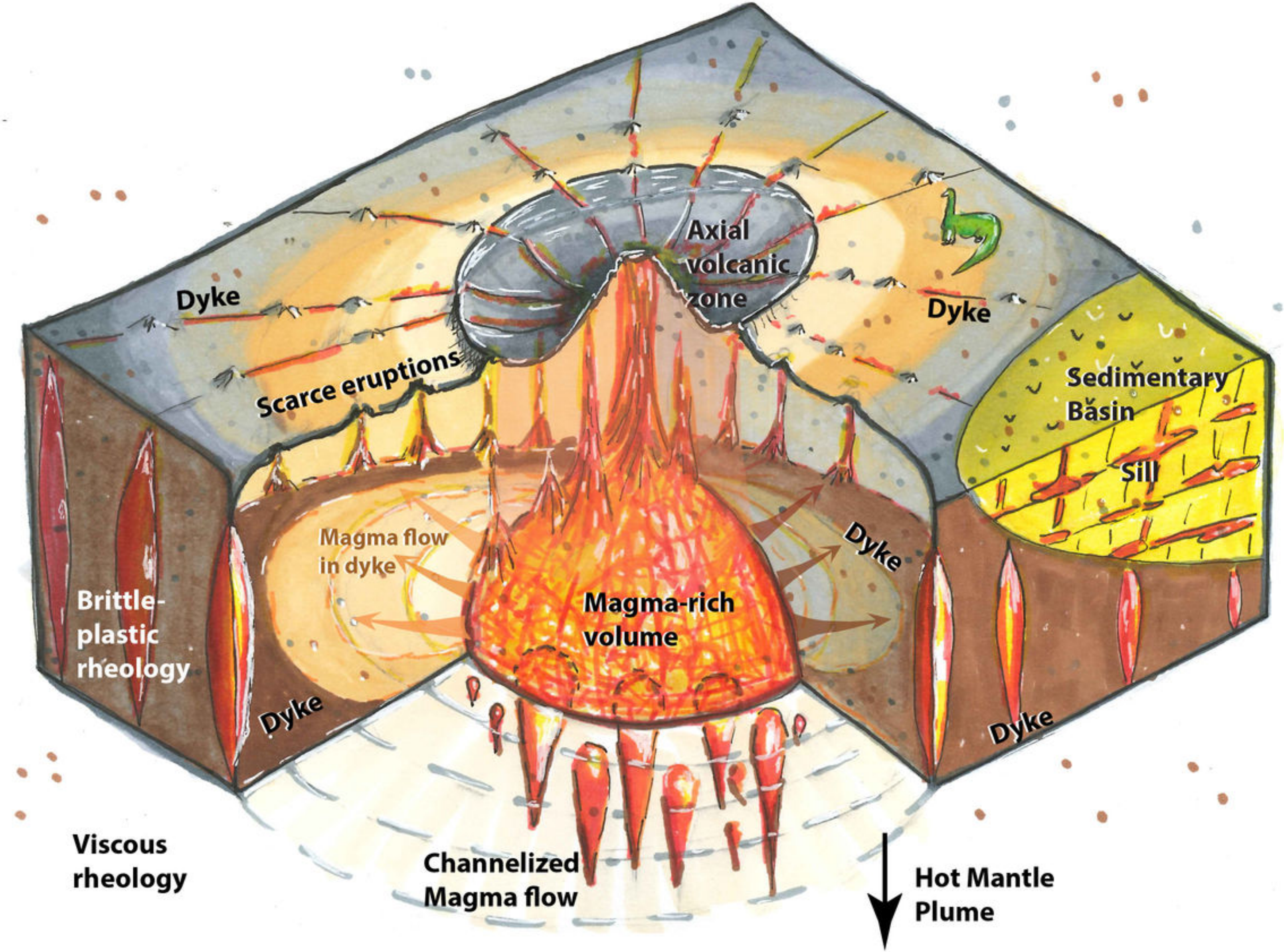
Axial volcanic zone
Dyke
Dyke
Scarce eruptions
Sedimentary Basin
Sill
Magma flow in dyke
Dyke
Magma-rich volume
Brittle-plastic rheology
Dyke
Dyke
Viscous rheology
Channelized Magma flow
Hot Mantle Plume

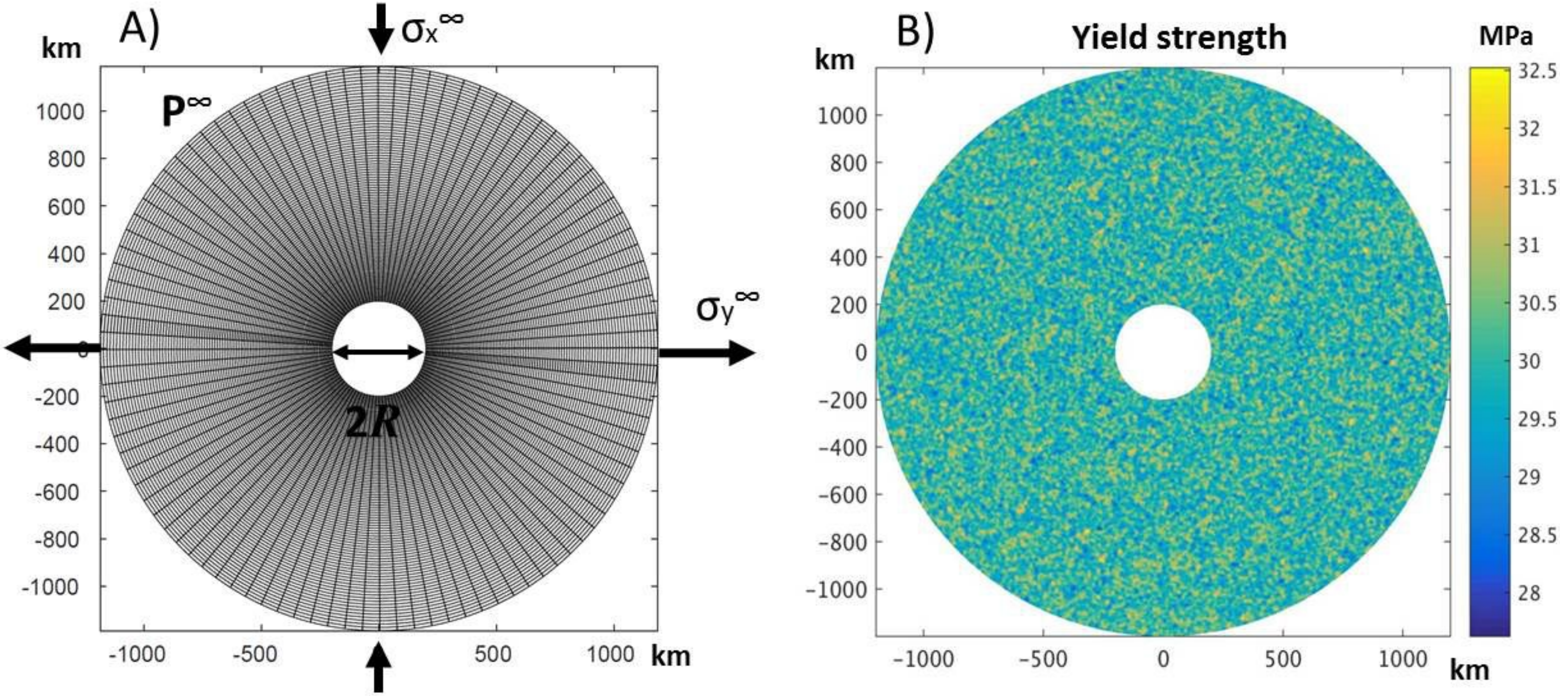
A)
σ_x^∞
km
P^∞
1000
800
600
400
200
0
-200
-400
-600
-800
-1000
σ_y^∞
$2R$
-1000
-500
500
1000
km
B)
Yield strength
MPa
km
32.5
32
31.5
31
30.5
30
29.5
29
28.5
28
1000
800
600
400
200
0
-200
-400
-600
-800
-1000
-1000
-500
0
500
1000
km

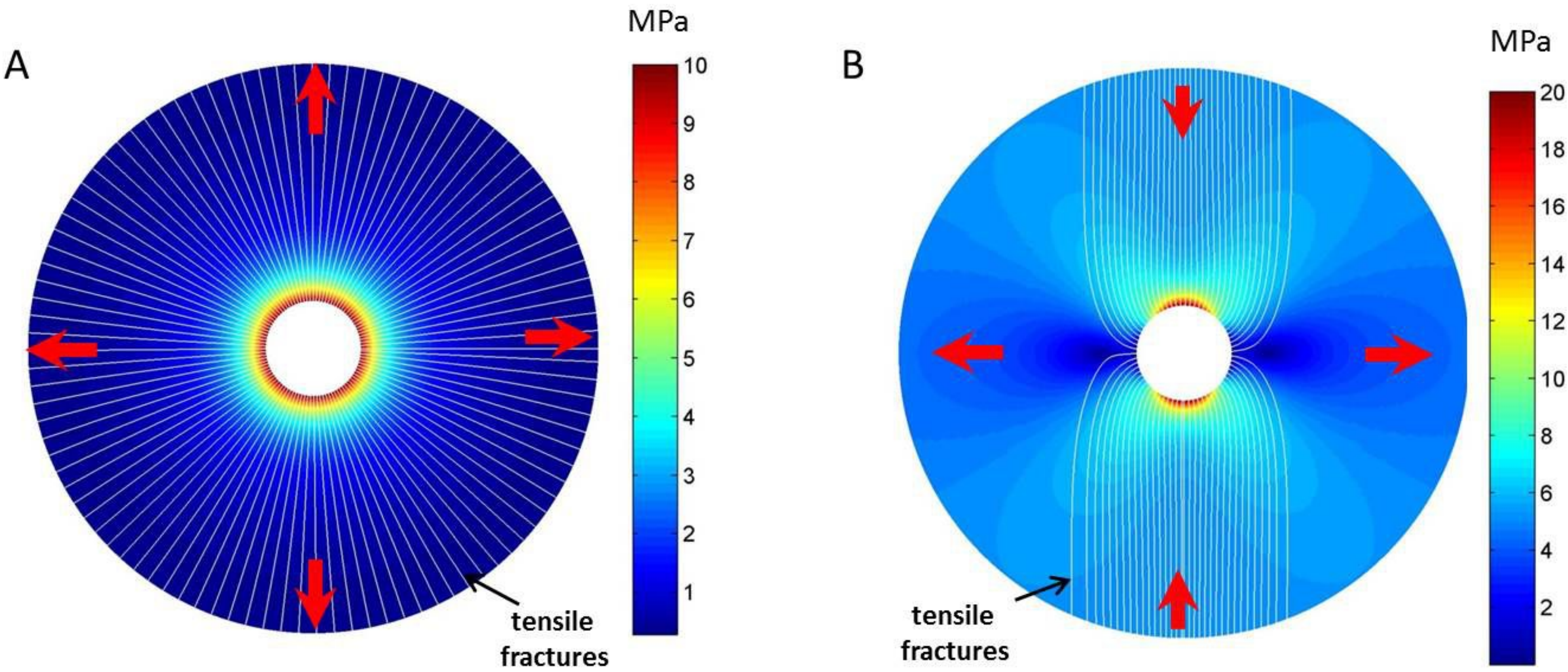

A
MPa
10
9
8
7
6
5
4
3
2
1
tensile
fractures
B
MPa
20
18
16
14
12
10
8
6
4
2
tensile
fractures

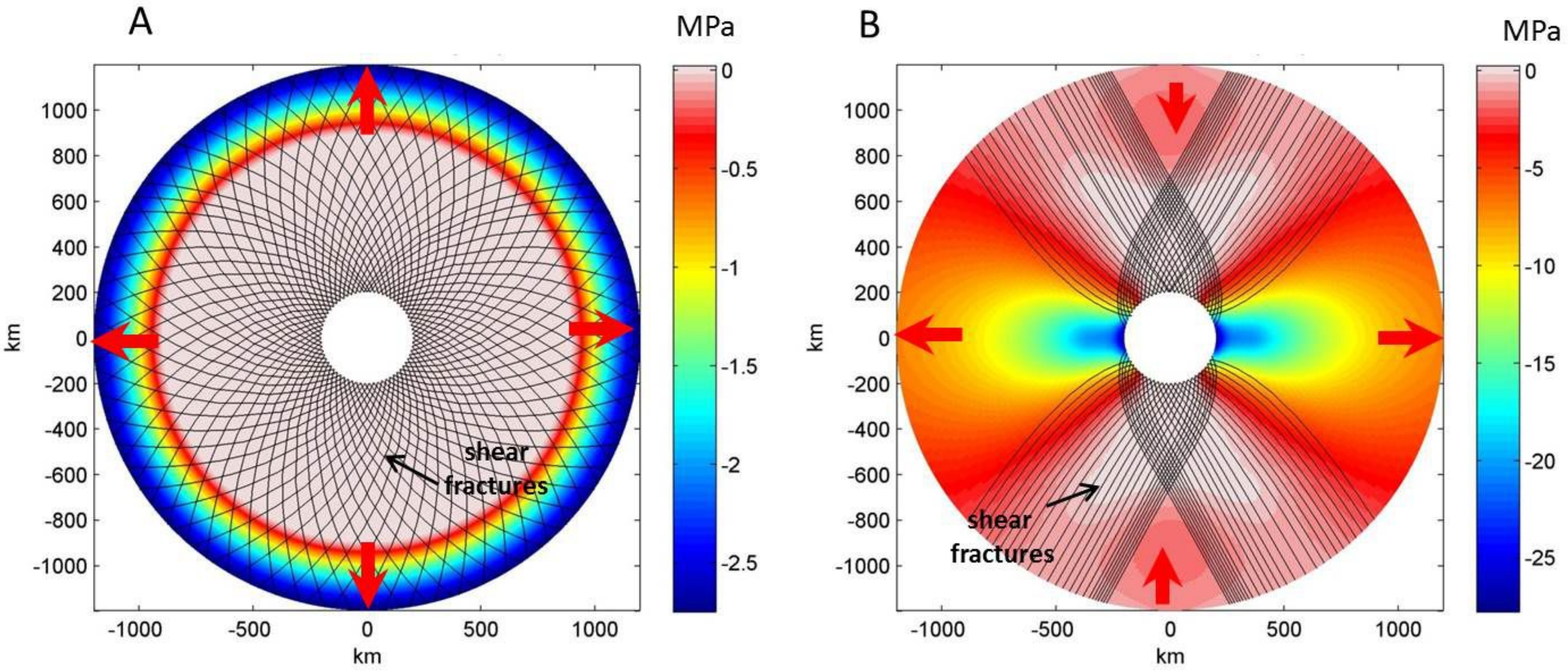

A
MPa
B
MPa
shear
fractures
shear
fractures
km
km
km
km
0
-0.5
-1
-1.5
-2
-2.5
0
-5
-10
-15
-20
-25
1000
800
600
400
200
0
-200
-400
-600
-800
-1000
-1000
-500
0
500
1000

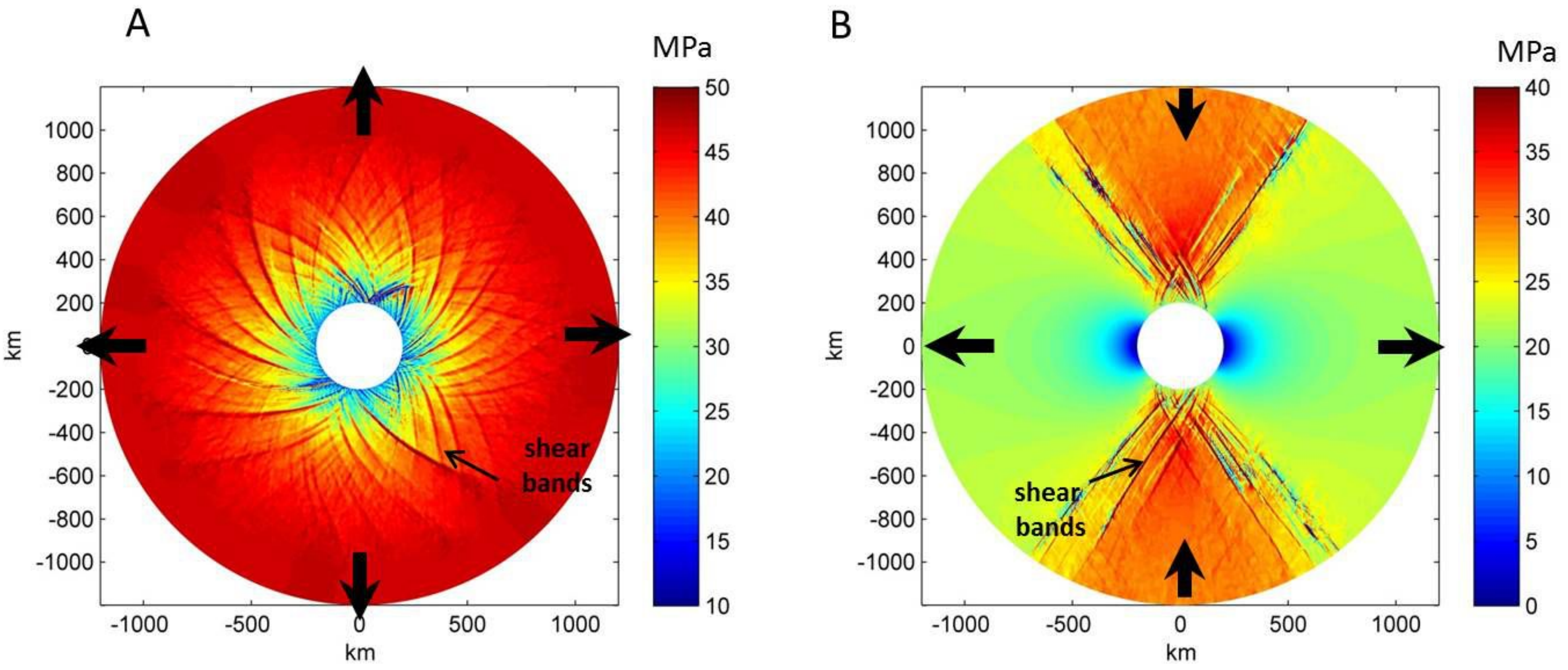

A
B
MPa
50
45
40
35
30
25
20
15
10
MPa
40
35
30
25
20
15
10
5
0
1000
800
600
400
200
0
-200
-400
-600
-800
-1000
km
-1000
-500
0
500
1000
km
shear
bands
shear
bands

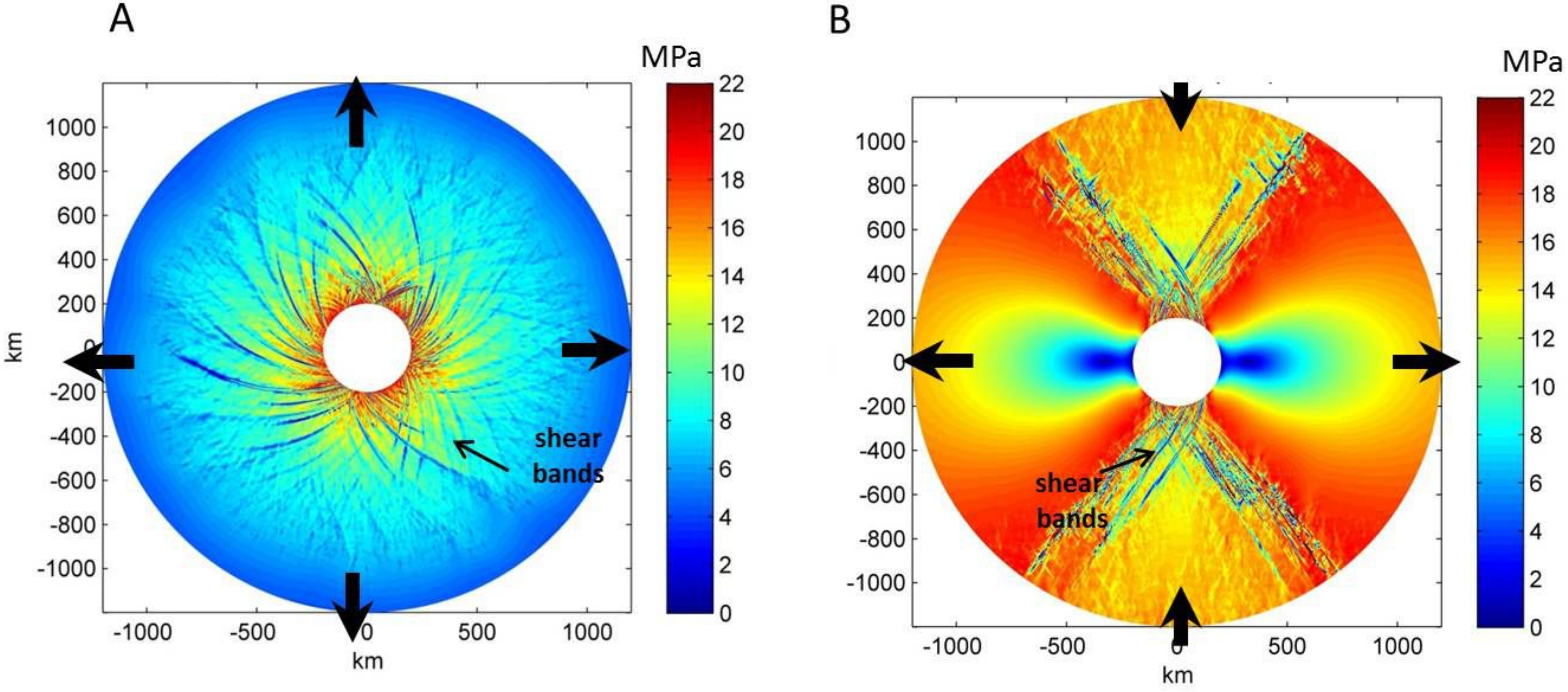

A
MPa
22
20
18
16
14
12
10
8
6
4
2
0
1000
800
600
400
200
0
-200
-400
-600
-800
-1000
km
-1000
-500
0
500
1000
km
shear bands
B
MPa
shear bands

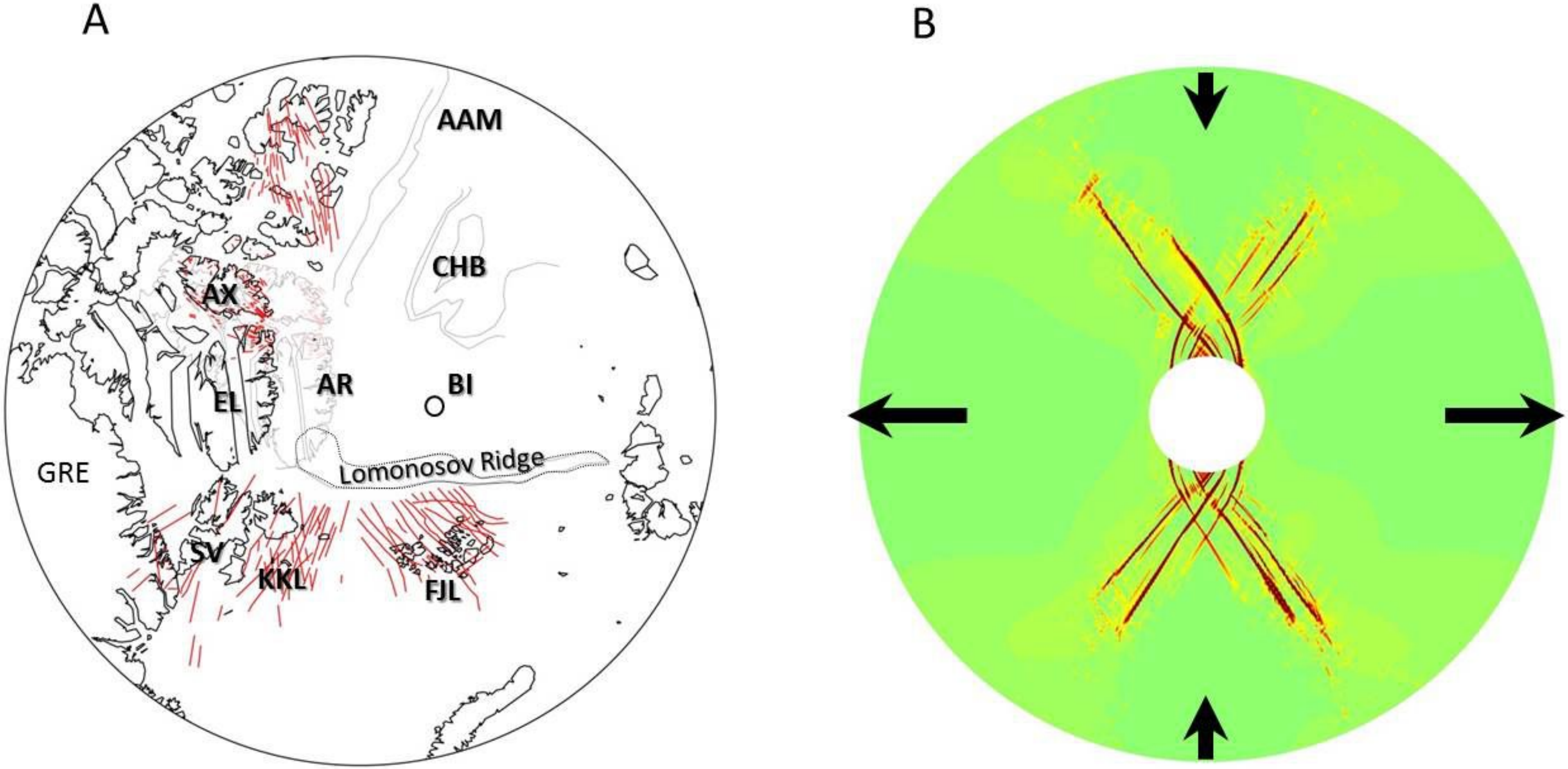
A
B
AAM
CHB
AX
AR
BI
EL
GRE
Lomonosov Ridge
SV
KKL
FJL

Parameter	**Value**
Shot point interval	37.5 m
Source depth	10 m
Streamer length	6000 m
Number of recording channels	480
Group interval	12.5 m
Nominal fold	80
Record length	12 s
Sampling rate	2 ms

Survey	Parameter	Value
Franz Josef Land	Trackline spacing	5 – 10 km
PMGRE (1997, 1998-2000)	RMS	5 nT
	Flight altitude	500-800 m
	Direction of tracklines	N-S
Svalbard	Trackline spacing	4 – 8 km
Sevmorgeo-PMGRE, TGS-NOPEC, NGU (1989-1991)	RMS	6-9 nT
	Flight altitude	250, 900, 1550 m
	Direction of tracklines	E-W